

20

Materials 2: the solid state

First, we see how to describe the regular arrangement of atoms in crystals and the symmetry of their arrangement. Then we consider the basic principles of X-ray diffraction and see how the diffraction pattern can be interpreted in terms of the distribution of electron density in a unit cell. X-ray diffraction leads to information about the structures of metallic, ionic, and molecular solids, and we review some typical results and their rationalization in terms of atomic and ionic radii. With structures established, we move on to the properties of solids, and see how their mechanical, electrical, optical, and magnetic properties stem from the properties of their constituent atoms and molecules.

The solid state includes most of the materials that make modern technology possible. It includes the wide varieties of steel that are used in architecture and engineering, the semiconductors and metallic conductors that are used in information technology and power distribution, the ceramics that increasingly are replacing metals, and the synthetic and natural polymers that are used in the textile industry and in the fabrication of many of the common objects of the modern world. The properties of solids stem, of course, from the arrangement and properties of the constituent atoms, and one of the challenges of this chapter is to see how a wide range of bulk properties, including rigidity, electrical conductivity, and optical and magnetic properties stem from the properties of atoms. One crucial aspect of this link is the pattern in which the atoms (and molecules) are stacked together, and we start this chapter with an examination of how the structures of solids are described and determined.

Crystal lattices

Early in the history of modern science it was suggested that the regular external form of crystals implied an internal regularity of their constituents. In this section we see how to describe the arrangement of atoms inside crystals.

20.1 Lattices and unit cells

A crystal is built up from regularly repeating ‘structural motifs’, which may be atoms, molecules, or groups of atoms, molecules, or ions. A **space lattice** is the pattern formed by points representing the locations of these motifs (Fig. 20.1). The space lattice is, in effect, an abstract scaffolding for the crystal structure. More formally, a space lattice is a three-dimensional, infinite array of points, each of which is surrounded in an identical way by its neighbours, and which defines the basic structure of the crystal. In some cases there may be a structural motif centred on each lattice

Crystal lattices

- 20.1 Lattices and unit cells
- 20.2 The identification of lattice planes
- 20.3 The investigation of structure
 - I20.1 Impact on biochemistry: X-ray crystallography of biological macromolecules
- 20.4 Neutron and electron diffraction

Crystal structure

- 20.5 Metallic solids
- 20.6 Ionic solids
- 20.7 Molecular solids and covalent networks

The properties of solids

- 20.8 Mechanical properties
- 20.9 Electrical properties
- I20.2 Impact on nanoscience: Nanowires
- 20.10 Optical properties
- 20.11 Magnetic properties
- 20.12 Superconductors

Checklist of key ideas

Further reading

Discussion questions

Exercises

Problems

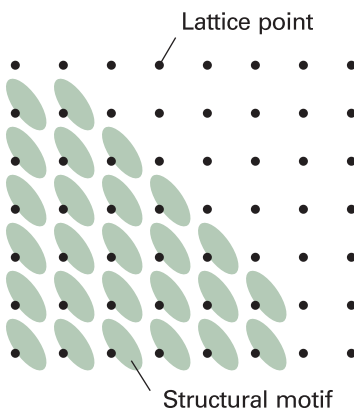


Fig. 20.1 Each lattice point specifies the location of a structural motif (for example, a molecule or a group of molecules). The crystal lattice is the array of lattice points; the crystal structure is the collection of structural motifs arranged according to the lattice.

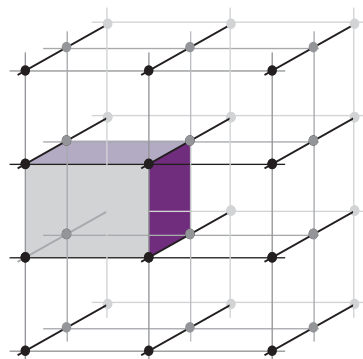


Fig. 20.2 A unit cell is a parallel-sided (but not necessarily rectangular) figure from which the entire crystal structure can be constructed by using only translations (not reflections, rotations, or inversions).

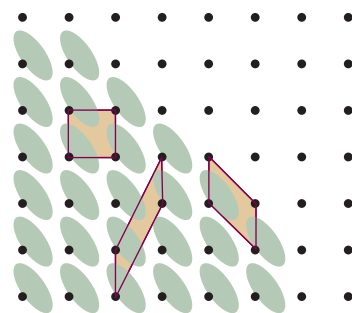


Fig. 20.3 A unit cell can be chosen in a variety of ways, as shown here. It is conventional to choose the cell that represents the full symmetry of the lattice. In this rectangular lattice, the rectangular unit cell would normally be adopted.

point, but that is not necessary. The crystal structure itself is obtained by associating with each lattice point an identical structural motif.

The **unit cell** is an imaginary parallelepiped (parallel-sided figure) that contains one unit of the translationally repeating pattern (Fig. 20.2). A unit cell can be thought of as the fundamental region from which the entire crystal may be constructed by purely translational displacements (like bricks in a wall). A unit cell is commonly formed by joining neighbouring lattice points by straight lines (Fig. 20.3). Such unit cells are called **primitive**. It is sometimes more convenient to draw larger **non-primitive unit cells** that also have lattice points at their centres or on pairs of opposite faces. An infinite number of different unit cells can describe the same lattice, but the one with sides that have the shortest lengths and that are most nearly perpendicular to one another is normally chosen. The lengths of the sides of a unit cell are denoted a , b , and c , and the angles between them are denoted α , β , and γ (Fig. 20.4).

Unit cells are classified into seven **crystal systems** by noting the rotational symmetry elements they possess. A **cubic unit cell**, for example, has four threefold axes in a tetrahedral array (Fig. 20.5). A **monoclinic unit cell** has one twofold axis; the unique

Comment 20.1

A **symmetry operation** is an action (such as a rotation, reflection, or inversion) that leaves an object looking the same after it has been carried out. There is a corresponding **symmetry element** for each symmetry operation, which is the point, line, or plane with respect to which the symmetry operation is performed. For instance, an n -fold rotation (the symmetry operation) about an n -fold axis of symmetry (the corresponding symmetry element) is a rotation through $360^\circ/n$. See Chapter 12 for a more detailed discussion of symmetry.

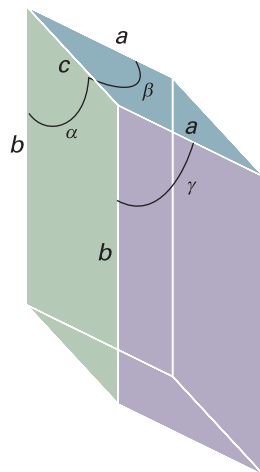


Fig. 20.4 The notation for the sides and angles of a unit cell. Note that the angle α lies in the plane (b,c) and perpendicular to the axis a .

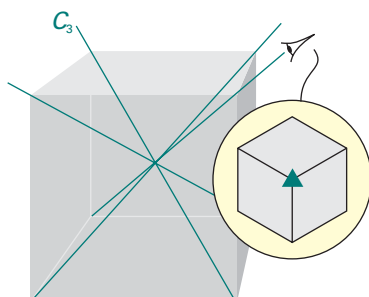


Fig. 20.5 A unit cell belonging to the cubic system has four threefold axes, denoted C_3 , arranged tetrahedrally. The insert shows the threefold symmetry.

axis is by convention the b axis (Fig. 20.6). A **triclinic unit cell** has no rotational symmetry, and typically all three sides and angles are different (Fig. 20.7). Table 20.1 lists the **essential symmetries**, the elements that must be present for the unit cell to belong to a particular crystal system.

There are only 14 distinct space lattices in three dimensions. These **Bravais lattices** are illustrated in Fig. 20.8. It is conventional to portray these lattices by primitive unit cells in some cases and by non-primitive unit cells in others. A **primitive unit cell** (with lattice points only at the corners) is denoted P. A **body-centred unit cell** (I) also has a lattice point at its centre. A **face-centred unit cell** (F) has lattice points at its corners and also at the centres of its six faces. A **side-centred unit cell** (A, B, or C) has lattice points at its corners and at the centres of two opposite faces. For simple structures, it is often convenient to choose an atom belonging to the structural motif, or the

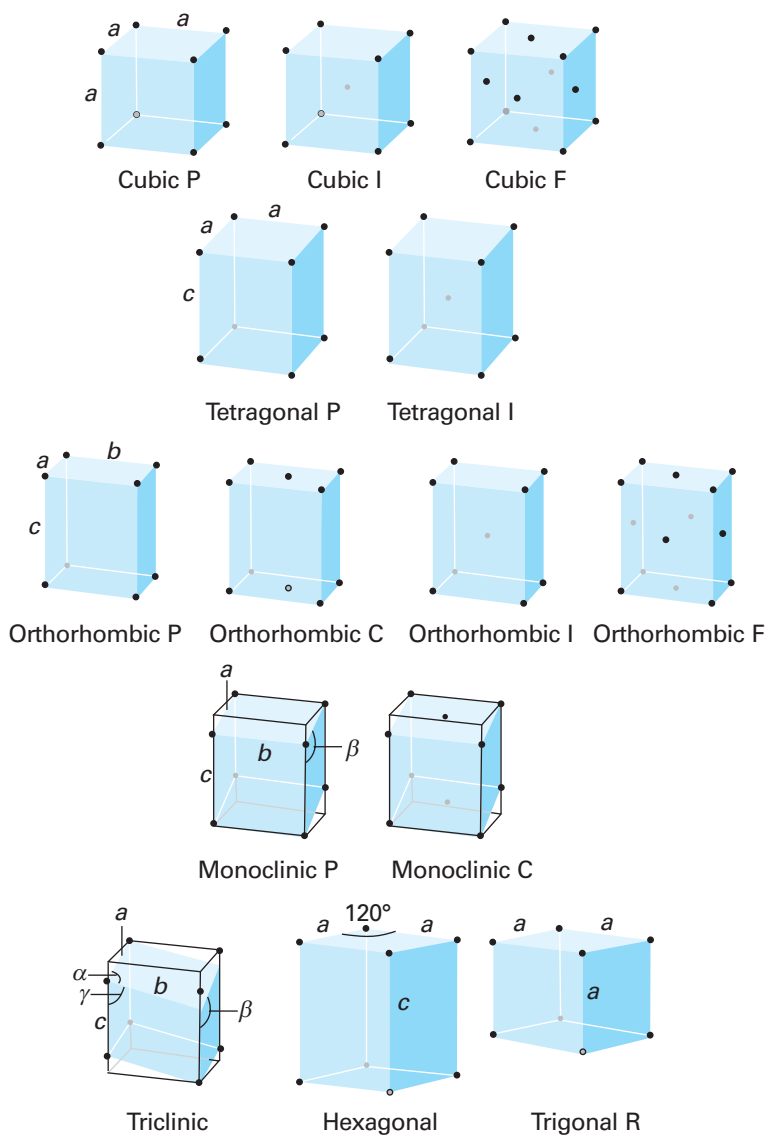


Fig. 20.8 The fourteen Bravais lattices. The points are lattice points, and are not necessarily occupied by atoms. P denotes a primitive unit cell (R is used for a trigonal lattice), I a body-centred unit cell, F a face-centred unit cell, and C (or A or B) a cell with lattice points on two opposite faces.

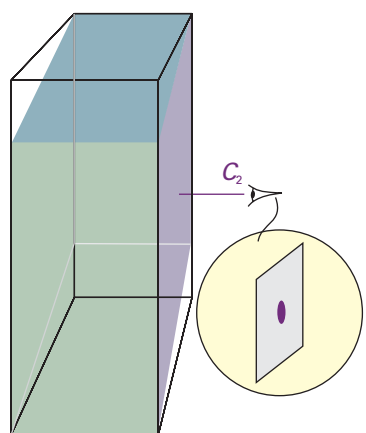


Fig. 20.6 A unit belonging to the monoclinic system has a two-fold axis (denoted C_2 and shown in more detail in the insert).

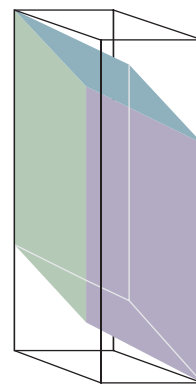


Fig. 20.7 A triclinic unit cell has no axes of rotational symmetry.

Table 20.1 The seven crystal systems

System	Essential symmetries
Triclinic	None
Monoclinic	One C_2 axis
Orthorhombic	Three perpendicular C_2 axes
Rhombohedral	One C_3 axis
Tetragonal	One C_4 axis
Hexagonal	One C_6 axis
Cubic	Four C_3 axes in a tetrahedral arrangement

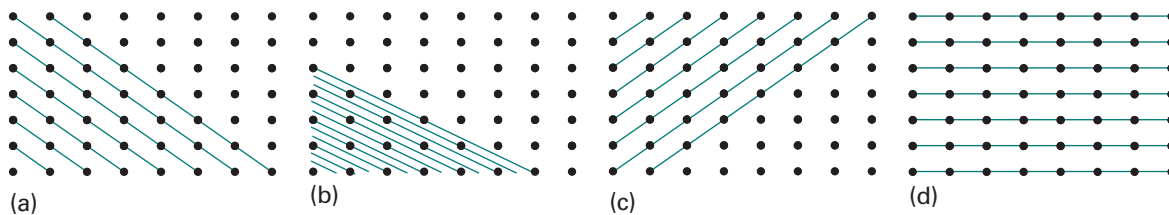


Fig. 20.9 Some of the planes that can be drawn through the points of a rectangular space lattice and their corresponding Miller indices (hkl): (a) (110), (b) (230), (c) ($\bar{1}10$), and (d) (010).

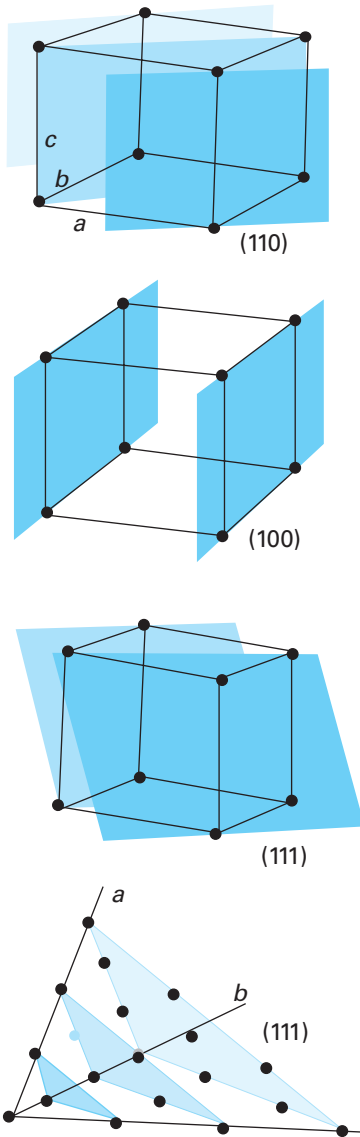


Fig. 20.10 Some representative planes in three dimensions and their Miller indices. Note that a 0 indicates that a plane is parallel to the corresponding axis, and that the indexing may also be used for unit cells with non-orthogonal axes.

centre of a molecule, as the location of a lattice point or the vertex of a unit cell, but that is not a necessary requirement.

20.2 The identification of lattice planes

The spacing of the planes of lattice points in a crystal is an important quantitative aspect of its structure. However, there are many different sets of planes (Fig. 20.9), and we need to be able to label them. Two-dimensional lattices are easier to visualize than three-dimensional lattices, so we shall introduce the concepts involved by referring to two dimensions initially, and then extend the conclusions by analogy to three dimensions.

(a) The Miller indices

Consider a two-dimensional rectangular lattice formed from a unit cell of sides a , b (as in Fig. 20.9). Each plane in the illustration (except the plane passing through the origin) can be distinguished by the distances at which it intersects the a and b axes. One way to label each set of parallel planes would therefore be to quote the smallest intersection distances. For example, we could denote the four sets in the illustration as $(1a, 1b)$, $(\frac{1}{2}a, \frac{1}{3}b)$, $(-1a, 1b)$, and $(\infty a, 1b)$. However, if we agree to quote distances along the axes as multiples of the lengths of the unit cell, then we can label the planes more simply as $(1, 1)$, $(\frac{1}{2}, \frac{1}{3})$, $(-1, 1)$, and $(\infty, 1)$. If the lattice in Fig. 20.9 is the top view of a three-dimensional orthorhombic lattice in which the unit cell has a length c in the z -direction, all four sets of planes intersect the z -axis at infinity. Therefore, the full labels are $(1, 1, \infty)$, $(\frac{1}{2}, \frac{1}{3}, \infty)$, $(-1, 1, \infty)$, and $(\infty, 1, \infty)$.

The presence of fractions and infinity in the labels is inconvenient. They can be eliminated by taking the reciprocals of the labels. As we shall see, taking reciprocals turns out to have further advantages. The **Miller indices**, (hkl) , are the reciprocals of intersection distances (with fractions cleared by multiplying through by an appropriate factor, if taking the reciprocal results in a fraction). For example, the $(1, 1, \infty)$ planes in Fig. 20.9a are the (110) planes in the Miller notation. Similarly, the $(\frac{1}{2}, \frac{1}{3}, \infty)$ planes are denoted (230) . Negative indices are written with a bar over the number, and Fig. 20.9c shows the $(\bar{1}10)$ planes. The Miller indices for the four sets of planes in Fig. 20.9 are therefore (110) , (230) , $(\bar{1}10)$, and (010) . Figure 20.10 shows a three-dimensional representation of a selection of planes, including one in a lattice with non-orthogonal axes.

The notation (hkl) denotes an *individual* plane. To specify a *set* of parallel planes we use the notation $\{hkl\}$. Thus, we speak of the (110) plane in a lattice, and the set of all $\{110\}$ planes that lie parallel to the (110) plane. A helpful feature to remember is that, the smaller the absolute value of h in $\{hkl\}$, the more nearly parallel the set of planes is to the a axis (the $\{h00\}$ planes are an exception). The same is true of k and the b axis and l and the c axis. When $h = 0$, the planes intersect the a axis at infinity, so the $\{0kl\}$

planes are parallel to the a axis. Similarly, the $\{h0l\}$ planes are parallel to b and the $\{hk0\}$ planes are parallel to c .

(b) The separation of planes

The Miller indices are very useful for expressing the separation of planes. The separation of the $\{hk0\}$ planes in the square lattice shown in Fig. 20.11 is given by

$$\frac{1}{d_{hk0}^2} = \frac{h^2 + k^2}{a^2} \quad \text{or} \quad d_{hk0} = \frac{a}{(h^2 + k^2)^{1/2}} \quad (20.1)$$

By extension to three dimensions, the separation of the $\{hkl\}$ planes of a cubic lattice is given by

$$\frac{1}{d_{hkl}^2} = \frac{h^2 + k^2 + l^2}{a^2} \quad \text{or} \quad d_{hkl} = \frac{a}{(h^2 + k^2 + l^2)^{1/2}} \quad (20.2)$$

The corresponding expression for a general orthorhombic lattice is the generalization of this expression:

$$\frac{1}{d_{hkl}^2} = \frac{h^2}{a^2} + \frac{k^2}{b^2} + \frac{l^2}{c^2} \quad (20.3)$$

Example 20.1 Using the Miller indices

Calculate the separation of (a) the $\{123\}$ planes and (b) the $\{246\}$ planes of an orthorhombic unit cell with $a = 0.82$ nm, $b = 0.94$ nm, and $c = 0.75$ nm.

Method For the first part, simply substitute the information into eqn 20.3. For the second part, instead of repeating the calculation, note that if all three Miller indices are multiplied by n , then their separation is reduced by that factor (Fig. 20.12):

$$\frac{1}{d_{nh,nk,nl}^2} = \frac{(nh)^2}{a^2} + \frac{(nk)^2}{b^2} + \frac{(nl)^2}{c^2} = n^2 \left(\frac{h^2}{a^2} + \frac{k^2}{b^2} + \frac{l^2}{c^2} \right) = \frac{n^2}{d_{hkl}^2}$$

which implies that

$$d_{nh,nk,nl} = \frac{d_{hkl}}{n}$$

Answer Substituting the indices into eqn 20.3 gives

$$\frac{1}{d_{123}^2} = \frac{1^2}{(0.82 \text{ nm})^2} + \frac{2^2}{(0.94 \text{ nm})^2} + \frac{3^2}{(0.75 \text{ nm})^2} = 0.22 \text{ nm}^{-2}$$

Hence, $d_{123} = 0.21$ nm. It then follows immediately that d_{246} is one-half this value, or 0.11 nm.

A note on good practice It is always sensible to look for analytical relations between quantities rather than to evaluate expressions numerically each time for that emphasizes the relations between quantities (and avoids unnecessary work).

Self-test 20.1 Calculate the separation of (a) the $\{133\}$ planes and (b) the $\{399\}$ planes in the same lattice. [0.19 nm, 0.063 nm]

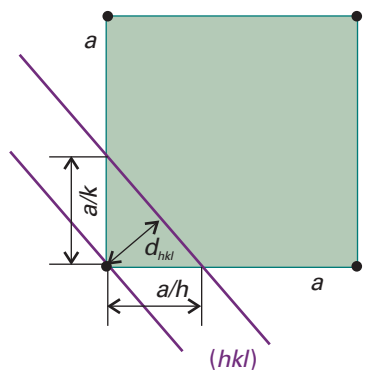


Fig. 20.11 The dimensions of a unit cell and their relation to the plane passing through the lattice points.

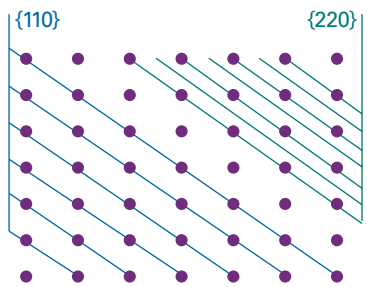


Fig. 20.12 The separation of the $\{220\}$ planes is half that of the $\{110\}$ planes. In general, (the separation of the planes $\{nh,nk,nl\}$) is n times smaller than the separation of the $\{hkl\}$ planes.

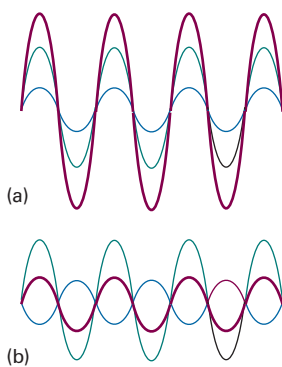


Fig. 20.13 When two waves are in the same region of space they interfere. Depending on their relative phase, they may interfere (a) constructively, to give an enhanced amplitude, or (b) destructively, to give a smaller amplitude. The component waves are shown in green and blue and the resultant in purple.

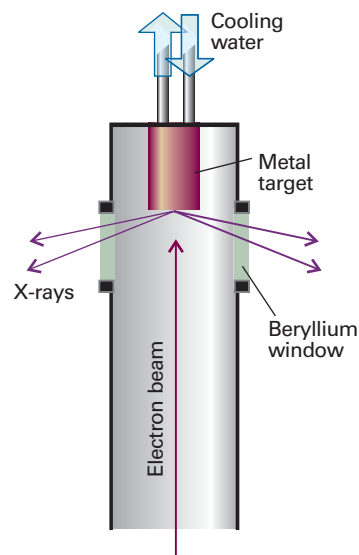


Fig. 20.14 X-rays are generated by directing an electron beam on to a cooled metal target. Beryllium is transparent to X-rays (on account of the small number of electrons in each atom) and is used for the windows.

20.3 The investigation of structure

A characteristic property of waves is that they interfere with one another, giving a greater displacement where peaks or troughs coincide and a smaller displacement where peaks coincide with troughs (Fig. 20.13). According to classical electromagnetic theory, the intensity of electromagnetic radiation is proportional to the square of the amplitude of the waves. Therefore, the regions of constructive or destructive interference show up as regions of enhanced or diminished intensities. The phenomenon of **diffraction** is the interference caused by an object in the path of waves, and the pattern of varying intensity that results is called the **diffraction pattern**. Diffraction occurs when the dimensions of the diffracting object are comparable to the wavelength of the radiation.

(a) X-ray diffraction

Wilhelm Röntgen discovered X-rays in 1895. Seventeen years later, Max von Laue suggested that they might be diffracted when passed through a crystal, for by then he had realized that their wavelengths are comparable to the separation of lattice planes. This suggestion was confirmed almost immediately by Walter Friedrich and Paul Knipping and has grown since then into a technique of extraordinary power. The bulk of this section will deal with the determination of structures using X-ray diffraction. The mathematical procedures necessary for the determination of structure from X-ray diffraction data are enormously complex, but such is the degree of integration of computers into the experimental apparatus that the technique is almost fully automated, even for large molecules and complex solids. The analysis is aided by molecular modelling techniques, which can guide the investigation towards a plausible structure.

X-rays are electromagnetic radiation with wavelengths of the order of 10^{-10} m. They are typically generated by bombarding a metal with high-energy electrons (Fig. 20.14). The electrons decelerate as they plunge into the metal and generate radiation with a continuous range of wavelengths called **Bremsstrahlung**.¹ Superimposed on the

¹ *Bremse* is German for deceleration, *Strahlung* for ray.

continuum are a few high-intensity, sharp peaks (Fig. 20.15). These peaks arise from collisions of the incoming electrons with the electrons in the inner shells of the atoms. A collision expels an electron from an inner shell, and an electron of higher energy drops into the vacancy, emitting the excess energy as an X-ray photon (Fig. 20.16). If the electron falls into a K shell (a shell with $n = 1$), the X-rays are classified as **K -radiation**, and similarly for transitions into the L ($n = 2$) and M ($n = 3$) shells. Strong, distinct lines are labelled K_{α} , K_{β} , and so on. Increasingly, X-ray diffraction makes use of the radiation available from synchrotron sources (*Further information 13.1*), for its high intensity greatly enhances the sensitivity of the technique.

von Laue's original method consisted of passing a broad-band beam of X-rays into a single crystal, and recording the diffraction pattern photographically. The idea behind the approach was that a crystal might not be suitably orientated to act as a diffraction grating for a single wavelength but, whatever its orientation, diffraction would be achieved for at least one of the wavelengths if a range of wavelengths was used. There is currently a resurgence of interest in this approach because synchrotron radiation spans a range of X-ray wavelengths.

An alternative technique was developed by Peter Debye and Paul Scherrer and independently by Albert Hull. They used monochromatic radiation and a powdered sample. When the sample is a powder, at least some of the crystallites will be orientated so as to give rise to diffraction. In modern powder diffractometers the intensities of the reflections are monitored electronically as the detector is rotated around the sample in a plane containing the incident ray (Fig. 20.17). Powder diffraction techniques are used to identify a sample of a solid substance by comparison of the positions of the diffraction lines and their intensities with diffraction patterns stored in a large data bank. Powder diffraction data are also used to determine phase diagrams, for different solid phases result in different diffraction patterns, and to determine the relative amounts of each phase present in a mixture. The technique is also used for the initial determination of the dimensions and symmetries of unit cells.

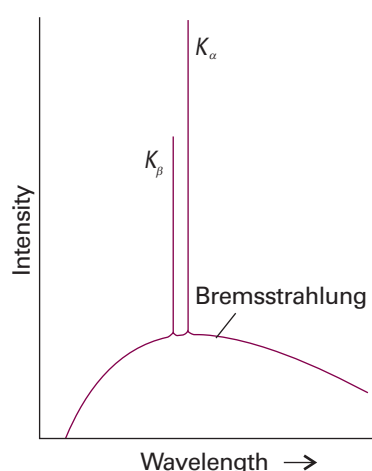


Fig. 20.15 The X-ray emission from a metal consists of a broad, featureless Bremsstrahlung background, with sharp transitions superimposed on it. The label K indicates that the radiation comes from a transition in which an electron falls into a vacancy in the K shell of the atom.

Comment 20.2
The web site contains links to databases of X-ray diffraction patterns.

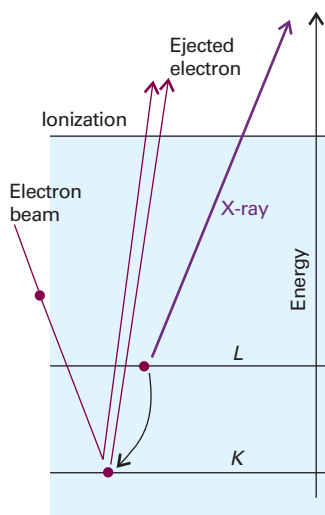


Fig. 20.16 The processes that contribute to the generation of X-rays. An incoming electron beam collides with an electron (in the K shell), and ejects it. Another electron (from the L shell in this illustration) falls into the vacancy and emits its excess energy as an X-ray photon.

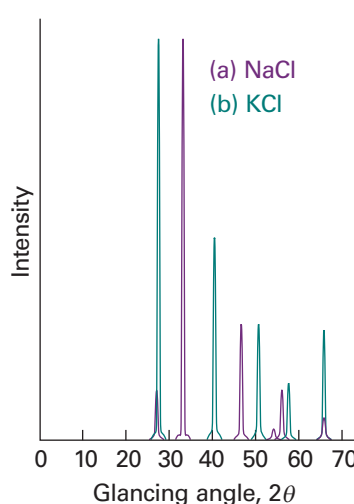


Fig. 20.17 X-ray powder photographs of (a) NaCl, (b) KCl and the indexed reflections. The smaller number of lines in (b) is a consequence of the similarity of the K^{+} and Cl^{-} scattering factors, as discussed later in the chapter.

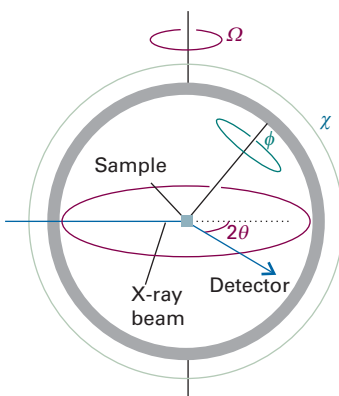


Fig. 20.18 A four-circle diffractometer. The settings of the orientations (ϕ , χ , θ , and Ω) of the components is controlled by computer; each (hkl) reflection is monitored in turn, and their intensities are recorded.

The method developed by the Braggs (William and his son Lawrence, who later jointly won the Nobel Prize) is the foundation of almost all modern work in X-ray crystallography. They used a single crystal and a monochromatic beam of X-rays, and rotated the crystal until a reflection was detected. There are many different sets of planes in a crystal, so there are many angles at which a reflection occurs. The complete set of data consists of the list of angles at which reflections are observed and their intensities.

Single-crystal diffraction patterns are measured by using a **four-circle diffractometer** (Fig. 20.18). The computer linked to the diffractometer determines the unit cell dimensions and the angular settings of the diffractometer's four circles that are needed to observe any particular intensity peak in the diffraction pattern. The computer controls the settings, and moves the crystal and the detector for each one in turn. At each setting, the diffraction intensity is measured, and background intensities are assessed by making measurements at slightly different settings. Computing techniques are now available that lead not only to automatic indexing but also to the automated determination of the shape, symmetry, and size of the unit cell. Moreover, several techniques are now available for sampling large amounts of data, including area detectors and image plates, which sample whole regions of diffraction patterns simultaneously.

(b) Bragg's law

An early approach to the analysis of diffraction patterns produced by crystals was to regard a lattice plane as a semi-transparent mirror, and to model a crystal as stacks of reflecting lattice planes of separation d (Fig. 20.19). The model makes it easy to calculate the angle the crystal must make to the incoming beam of X-rays for constructive interference to occur. It has also given rise to the name **reflection** to denote an intense beam arising from constructive interference.

Consider the reflection of two parallel rays of the same wavelength by two adjacent planes of a lattice, as shown in Fig. 20.19. One ray strikes point D on the upper plane but the other ray must travel an additional distance AB before striking the plane immediately below. Similarly, the reflected rays will differ in path length by a distance BC. The net path length difference of the two rays is then

$$AB + BC = 2d \sin \theta$$

where θ is the **glancing angle**. For many glancing angles the path-length difference is not an integer number of wavelengths, and the waves interfere largely destructively. However, when the path-length difference is an integer number of wavelengths ($AB + BC = n\lambda$), the reflected waves are in phase and interfere constructively. It follows that a reflection should be observed when the glancing angle satisfies **Bragg's law**:

$$n\lambda = 2d \sin \theta \quad (20.4)$$

Reflections with $n = 2, 3, \dots$ are called second-order, third-order, and so on; they correspond to path-length differences of 2, 3, ... wavelengths. In modern work it is normal to absorb the n into d , to write the Bragg law as

$$\lambda = 2d \sin \theta \quad (20.5)$$

and to regard the n th-order reflection as arising from the $\{nh, nk, nl\}$ planes (see Example 20.1).

The primary use of Bragg's law is in the determination of the spacing between the layers in the lattice for, once the angle θ corresponding to a reflection has been determined, d may readily be calculated.

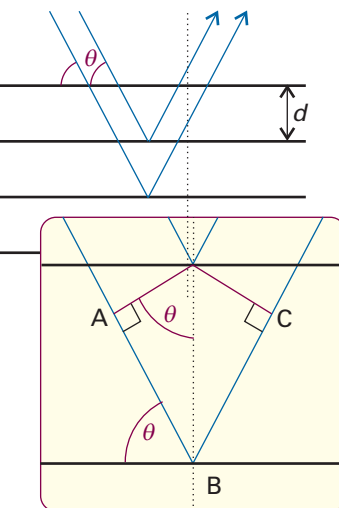


Fig. 20.19 The conventional derivation of Bragg's law treats each lattice plane as a reflecting the incident radiation. The path lengths differ by $AB + BC$, which depends on the glancing angle, θ . Constructive interference (a 'reflection') occurs when $AB + BC$ is equal to an integer number of wavelengths.

Example 20.2 Using Bragg's law

A first-order reflection from the {111} planes of a cubic crystal was observed at a glancing angle of 11.2° when $\text{Cu}(K_\alpha)$ X-rays of wavelength 154 pm were used. What is the length of the side of the unit cell?

Method The separation of the planes can be determined from Bragg's law. Because the crystal is cubic, the separation is related to the length of the side of the unit cell, a , by eqn 20.2, which may therefore be solved for a .

Answer According to eqn 20.5, the {111} planes responsible for the diffraction have separation

$$d_{111} = \frac{\lambda}{2 \sin \theta}$$

The separation of the {111} planes of a cubic lattice of side a is given by eqn 20.2 as

$$d_{111} = \frac{a}{3^{1/2}}$$

Therefore,

$$a = \frac{3^{1/2}\lambda}{2 \sin \theta} = \frac{3^{1/2} \times (154 \text{ pm})}{2 \sin 11.2^\circ} = 687 \text{ pm}$$

Self-test 20.2 Calculate the angle at which the same crystal will give a reflection from the {123} planes. [24.8°]

Some types of unit cell give characteristic and easily recognizable patterns of lines. For example, in a cubic lattice of unit cell dimension a the spacing is given by eqn 20.2, so the angles at which the $\{hkl\}$ planes give first-order reflections are given by

$$\sin \theta = (h^2 + k^2 + l^2)^{1/2} \frac{\lambda}{2a}$$

The reflections are then predicted by substituting the values of h , k , and l :

{100}	{110}	{111}	{200}	{210}	{211}	{220}	{300}	{221}	{310}	...
$h^2+k^2+l^2$	1	2	3	4	5	6	8	9	9	10...

Notice that 7 (and 15, ...) is missing because the sum of the squares of three integers cannot equal 7 (or 15, ...). Therefore the pattern has absences that are characteristic of the cubic P lattice.

Self-test 20.3 Normally, experimental procedures measure 2θ rather than θ itself. A diffraction examination of the element polonium gave lines at the following values of 2θ (in degrees) when 71.0 pm Mo X-rays were used: 12.1, 17.1, 21.0, 24.3, 27.2, 29.9, 34.7, 36.9, 38.9, 40.9, 42.8. Identify the unit cell and determine its dimensions. [cubic P; $a = 337 \text{ pm}$]

(c) Scattering factors

To prepare the way to discussing modern methods of structural analysis we need to note that the scattering of X-rays is caused by the oscillations an incoming electromagnetic

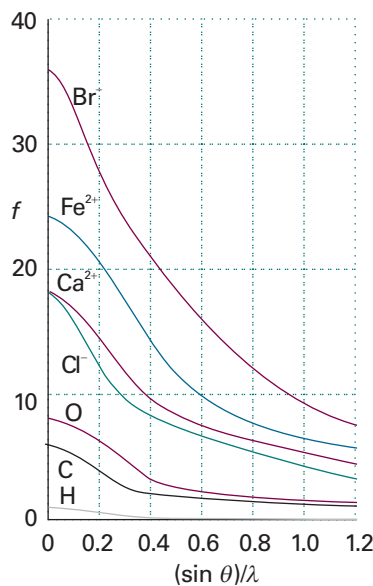


Fig. 20.20 The variation of the scattering factor of atoms and ions with atomic number and angle. The scattering factor in the forward direction (at $\theta=0$, and hence at $(\sin \theta)/\lambda=0$) is equal to the number of electrons present in the species.

wave generates in the electrons of atoms, and heavy atoms give rise to stronger scattering than light atoms. This dependence on the number of electrons is expressed in terms of the **scattering factor**, f , of the element. If the scattering factor is large, then the atoms scatter X-rays strongly. The scattering factor of an atom is related to the electron density distribution in the atom, $\rho(r)$, by

$$f = 4\pi \int_0^\infty \rho(r) \frac{\sin kr}{kr} r^2 dr \quad k = \frac{4\pi}{\lambda} \sin \theta \quad (20.6)$$

The value of f is greatest in the forward direction and smaller for directions away from the forward direction (Fig. 20.20). The detailed analysis of the intensities of reflections must take this dependence on direction into account (in single crystal studies as well as for powders). We show in the *Justification* below that, in the forward direction (for $\theta=0$), f is equal to the total number of electrons in the atom.

Justification 20.1 The forward scattering factor

As $\theta \rightarrow 0$, so $k \rightarrow 0$. Because $\sin x = x - \frac{1}{6}x^3 + \dots$,

$$\lim_{x \rightarrow 0} \frac{\sin x}{x} = \lim_{x \rightarrow 0} \frac{x - \frac{1}{6}x^3 + \dots}{x} = \lim_{x \rightarrow 0} (1 - \frac{1}{6}x^2 + \dots) = 1$$

The factor $(\sin kr)/kr$ is therefore equal to 1 for forward scattering. It follows that in the forward direction

$$f = 4\pi \int_0^\infty \rho(r) r^2 dr$$

The integral over the electron density ρ (the number of electrons in an infinitesimal region divided by the volume of the region) multiplied by the volume element $4\pi r^2 dr$ is the total number of electrons, N_e , in the atom. Hence, in the forward direction, $f = N_e$. For example, the scattering factors of Na^+ , K^+ , and Cl^- are 8, 18, and 18, respectively.

The scattering factor is smaller in nonforward directions because $(\sin kr)/kr < 1$ for $\theta > 0$, so the integral is smaller than the value calculated above.

(d) The electron density

The problem we now address is how to interpret the data from a diffractometer in terms of the detailed structure of a crystal. To do so, we must go beyond Bragg's law.

If a unit cell contains several atoms with scattering factors f_j and coordinates $(x_j a, y_j b, z_j c)$, then we show in the *Justification* below that the overall amplitude of a wave diffracted by the $\{hkl\}$ planes is given by

$$F_{hkl} = \sum_j f_j e^{i\phi_{hkl}(j)} \quad \text{where} \quad \phi_{hkl}(j) = 2\pi(hx_j + ky_j + lz_j) \quad (20.7)$$

The sum is over all the atoms in the unit cell. The quantity F_{hkl} is called the **structure factor**.

Justification 20.2 The structure factor

We begin by showing that, if in the unit cell there is an A atom at the origin and a B atom at the coordinates (xa, yb, zc) , where x, y , and z lie in the range 0 to 1, then the phase difference, ϕ , between the hkl reflections of the A and B atoms is $\phi_{hkl} = 2\pi(hx + ky + lz)$.

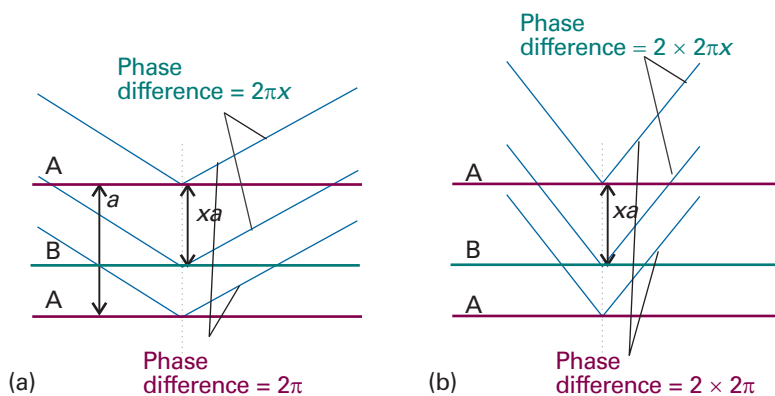


Fig. 20.21 Diffraction from a crystal containing two kinds of atoms. (a) For a (100) reflection from the A planes, there is a phase difference of 2π between waves reflected by neighbouring planes. (b) For a (200) reflection, the phase difference is 4π . The reflection from a B plane at a fractional distance xa from an A plane has a phase that is x times these phase differences.

Consider the crystal shown schematically in Fig. 20.21. The reflection corresponds to two waves from adjacent A planes, the phase difference of the waves being 2π . If there is a B atom at a fraction x of the distance between the two A planes, then it gives rise to a wave with a phase difference $2\pi x$ relative to an A reflection. To see this conclusion, note that, if $x = 0$, there is no phase difference; if $x = \frac{1}{2}$ the phase difference is π ; if $x = 1$, the B atom lies where the lower A atom is and the phase difference is 2π . Now consider a (200) reflection. There is now a $2 \times 2\pi$ difference between the waves from the two A layers, and if B were to lie at $x = 0.5$ it would give rise to a wave that differed in phase by 2π from the wave from the upper A layer. Thus, for a general fractional position x , the phase difference for a (200) reflection is $2 \times 2\pi x$. For a general $(h00)$ reflection, the phase difference is therefore $h \times 2\pi x$. For three dimensions, this result generalizes to eqn 20.7.

The A and B reflections interfere destructively when the phase difference is π , and the total intensity is zero if the atoms have the same scattering power. For example, if the unit cells are cubic I with a B atom at $x = y = z = \frac{1}{2}$, then the A,B phase difference is $(h + k + l)\pi$. Therefore, all reflections for odd values of $h + k + l$ vanish because the waves are displaced in phase by π . Hence the diffraction pattern for a cubic I lattice can be constructed from that for the cubic P lattice (a cubic lattice without points at the centre of its unit cells) by striking out all reflections with odd values of $h + k + l$. Recognition of these **systematic absences** in a powder spectrum immediately indicates a cubic I lattice (Fig. 20.22).

If the amplitude of the waves scattered from A is f_A at the detector, that of the waves scattered from B is $f_B e^{i\phi_{hkl}}$, with ϕ_{hkl} the phase difference given in eqn 20.7. The total amplitude at the detector is therefore

$$F_{hkl} = f_A + f_B e^{i\phi_{hkl}}$$

Because the intensity is proportional to the square modulus of the amplitude of the wave, the intensity, I_{hkl} , at the detector is

$$I_{hkl} \propto F_{hkl}^* F_{hkl} = (f_A + f_B e^{-i\phi_{hkl}})(f_A + f_B e^{i\phi_{hkl}})$$

This expression expands to

$$I_{hkl} \propto f_A^2 + f_B^2 + f_A f_B (e^{i\phi_{hkl}} + e^{-i\phi_{hkl}}) = f_A^2 + f_B^2 + 2f_A f_B \cos \phi_{hkl}$$

The cosine term either adds to or subtracts from $f_A^2 + f_B^2$ depending on the value of ϕ_{hkl} , which in turn depends on h , k , and l and x , y , and z . Hence, there is a variation in the intensities of the lines with different hkl .

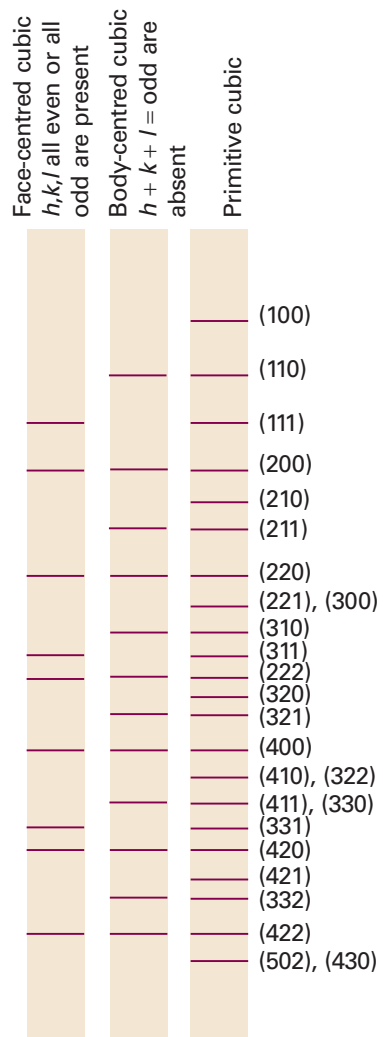


Fig. 20.22 The powder diffraction patterns and the systematic absences of three versions of a cubic cell. Comparison of the observed pattern with patterns like these enables the unit cell to be identified. The locations of the lines give the cell dimensions.

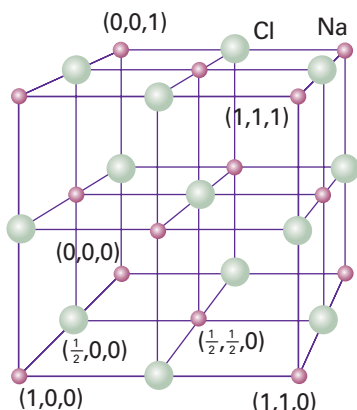


Fig. 20.23 The location of the atoms for the structure factor calculation in Example 20.3. The purple circles are Na^+ ; the green circles are Cl^- .

Example 20.3 Calculating a structure factor

Calculate the structure factors for the unit cell in Fig. 20.23.

Method The structure factor is defined by eqn 20.7. To use this equation, consider the ions at the locations specified in Fig. 20.23. Write f^+ for the Na^+ scattering factor and f^- for the Cl^- scattering factor. Note that ions in the body of the cell contribute to the scattering with a strength f . However, ions on faces are shared between two cells (use $\frac{1}{2}f$), those on edges by four cells (use $\frac{1}{4}f$), and those at corners by eight cells (use $\frac{1}{8}f$). Two useful relations are

$$e^{i\pi} = -1 \quad \cos \phi = \frac{1}{2}(e^{i\phi} + e^{-i\phi})$$

Answer From eqn 20.7, and summing over the coordinates of all 27 atoms in the illustration:

$$F_{hkl} = f^+\left(\frac{1}{8} + \frac{1}{8}e^{2\pi i l} + \dots + \frac{1}{2}e^{2\pi i (\frac{1}{2}h + \frac{1}{2}k + \frac{1}{2}l)}\right) \\ + f^-\left(e^{2\pi i (\frac{1}{2}h + \frac{1}{2}k + \frac{1}{2}l)} + \frac{1}{4}e^{2\pi i (\frac{1}{2}h)} + \dots + \frac{1}{4}e^{2\pi i (\frac{1}{2}h + l)}\right)$$

To simplify this 27-term expression, we use

$$e^{2\pi i h} = e^{2\pi i k} = e^{2\pi i l} = 1$$

because h , k , and l are all integers:

$$F_{hkl} = f^+\{1 + \cos(h+k)\pi + \cos(h+l)\pi + \cos(k+l)\pi\} \\ + f^-\{(-1)^{h+k+l} + \cos k\pi + \cos l\pi + \cos h\pi\}$$

Then, because $\cos h\pi = (-1)^h$,

$$F_{hkl} = f^+\{1 + (-1)^{h+k} + (-1)^{h+l} + (-1)^{l+k}\} + f^-\{(-1)^{h+k+l} + (-1)^h + (-1)^k + (-1)^l\}$$

Now note that:

$$\begin{aligned} \text{if } h, k, \text{ and } l \text{ are all even, } F_{hkl} &= f^+\{1 + 1 + 1 + 1\} + f^-\{1 + 1 + 1 + 1\} = 4(f^+ + f^-) \\ \text{if } h, k, \text{ and } l \text{ are all odd, } F_{hkl} &= 4(f^+ - f^-) \end{aligned}$$

$$\text{if one index is odd and two are even, or vice versa, } F_{hkl} = 0$$

The hkl all-odd reflections are less intense than the hkl all-even. For $f^+ = f^-$, which is the case for identical atoms in a cubic P arrangement, the hkl all-odd have zero intensity, corresponding to the ‘systematic absences’ of cubic P unit cells.

Self-test 20.4 Which reflections cannot be observed for a cubic I lattice?

$$[\text{for } h+k+l \text{ odd, } F_{hkl} = 0]$$

The intensity of the (hkl) reflection is proportional to $|F_{hkl}|^2$, so in principle we can determine the structure factors experimentally by taking the square root of the corresponding intensities (but see below). Then, once we know all the structure factors F_{hkl} , we can calculate the electron density distribution, $\rho(\mathbf{r})$, in the unit cell by using the expression

$$\rho(\mathbf{r}) = \frac{1}{V} \sum_{hkl} F_{hkl} e^{-2\pi i (hx + ky + lz)} \quad (20.8)$$

where V is the volume of the unit cell. Equation 20.8 is called a **Fourier synthesis** of the electron density.

Example 20.4 Calculating an electron density by Fourier synthesis

Consider the $\{h00\}$ planes of a crystal extending indefinitely in the x -direction. In an X-ray analysis the structure factors were found as follows:

$h:$	0	1	2	3	4	5	6	7	8	9
F_h	16	-10	2	-1	7	-10	8	-3	2	-3
$h:$	10	11	12	13	14	15				
F_h	6	-5	3	-2	2	-3				

(and $F_{-h} = F_h$). Construct a plot of the electron density projected on to the x -axis of the unit cell.

Method Because $F_{-h} = F_h$, it follows from eqn 20.8 that

$$\begin{aligned} V\rho(x) &= \sum_{h=-\infty}^{\infty} F_h e^{-2\pi i h x} = F_0 + \sum_{h=1}^{\infty} (F_h e^{-2\pi i h x} + F_{-h} e^{2\pi i h x}) \\ &= F_0 + \sum_{h=1}^{\infty} F_h (e^{-2\pi i h x} + e^{2\pi i h x}) = F_0 + 2 \sum_{h=1}^{\infty} F_h \cos 2\pi h x \end{aligned}$$

and we evaluate the sum (truncated at $h = 15$) for points $0 \leq x \leq 1$ using mathematical software.

Answer The results are plotted in Fig. 20.24 (blue line). The positions of three atoms can be discerned very readily. The more terms there are included, the more accurate the density plot. Terms corresponding to high values of h (short wavelength cosine terms in the sum) account for the finer details of the electron density; low values of h account for the broad features.

Self-test 20.5 Use mathematical software to experiment with different structure factors (including changing signs as well as amplitudes). For example, use the same values of F_h as above, but with positive signs for $h \geq 6$.

[Fig. 20.24 (purple line)]

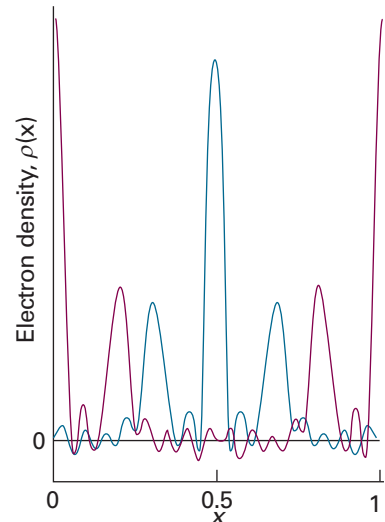


Fig. 20.24 The plot of the electron density calculated in Example 20.4 (blue) and Self-test 20.5 (purple).

 **Exploration** If you do not have access to mathematical software, perform the calculations suggested in Self-test 20.5 by using the interactive applets found in the text's web site.

(e) The phase problem

A problem with the procedure outlined above is that the observed intensity I_{hkl} is proportional to the square modulus $|F_{hkl}|^2$, so we cannot say whether we should use $+|F_{hkl}|$ or $-|F_{hkl}|$ in the sum in eqn 20.8. In fact, the difficulty is more severe for non-centrosymmetric unit cells because, if we write F_{hkl} as the complex number $|F_{hkl}|e^{i\alpha}$, where α is the phase of F_{hkl} and $|F_{hkl}|$ is its magnitude, then the intensity lets us determine $|F_{hkl}|$ but tells us nothing of its phase, which may lie anywhere from 0 to 2π . This ambiguity is called the **phase problem**; its consequences are illustrated by comparing the two plots in Fig. 20.24. Some way must be found to assign phases to the structure factors, for otherwise the sum for ρ cannot be evaluated and the method would be useless.

The phase problem can be overcome to some extent by a variety of methods. One procedure that is widely used for inorganic materials with a reasonably small number of atoms in a unit cell and for organic molecules with a small number of heavy atoms is the **Patterson synthesis**. Instead of the structure factors F_{hkl} , the values of $|F_{hkl}|^2$, which can be obtained without ambiguity from the intensities, are used in an expression that resembles eqn 20.8:

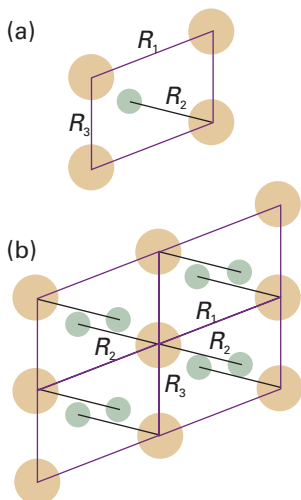


Fig. 20.25 The Patterson synthesis corresponding to the pattern in (a) is the pattern in (b). The distance and orientation of each spot from the origin gives the orientation and separation of one atom–atom separation in (a). Some of the typical distances and their contribution to (b) are shown as R_1 , etc.

$$P(\mathbf{r}) = \frac{1}{V} \sum_{hkl} |F_{hkl}|^2 e^{-2\pi i(hx+ky+lz)} \quad (20.9)$$

The outcome of a Patterson synthesis is a map of the vector separations of the atoms (the distances and directions between atoms) in the unit cell. Thus, if atom A is at the coordinates (x_A, y_A, z_A) and atom B is at (x_B, y_B, z_B) , then there will be a peak at $(x_A - x_B, y_A - y_B, z_A - z_B)$ in the Patterson map. There will also be a peak at the negative of these coordinates, because there is a vector from B to A as well as a vector from A to B. The height of the peak in the map is proportional to the product of the atomic numbers of the two atoms, $Z_A Z_B$. For example, if the unit cell has the structure shown in Fig. 20.25a, the Patterson synthesis would be the map shown in Fig. 20.25b, where the location of each spot relative to the origin gives the separation and relative orientation of each pair of atoms in the original structure.

Heavy atoms dominate the scattering because their scattering factors are large, of the order of their atomic numbers, and their locations may be deduced quite readily. The sign of F_{hkl} can now be calculated from the locations of the heavy atoms in the unit cell, and to a high probability the phase calculated for them will be the same as the phase for the entire unit cell. To see why this is so, we have to note that a structure factor of a centrosymmetric cell has the form

$$F = (\pm)f_{\text{heavy}} + (\pm)f_{\text{light}} + (\pm)f_{\text{light}} + \dots \quad (20.10)$$

where f_{heavy} is the scattering factor of the heavy atom and f_{light} the scattering factors of the light atoms. The f_{light} are all much smaller than f_{heavy} , and their phases are more or less random if the atoms are distributed throughout the unit cell. Therefore, the net effect of the f_{light} is to change F only slightly from f_{heavy} , and we can be reasonably confident that F will have the same sign as that calculated from the location of the heavy atom. This phase can then be combined with the observed $|F|$ (from the reflection intensity) to perform a Fourier synthesis of the full electron density in the unit cell, and hence to locate the light atoms as well as the heavy atoms.

Modern structural analyses make extensive use of **direct methods**. Direct methods are based on the possibility of treating the atoms in a unit cell as being virtually randomly distributed (from the radiation's point of view), and then using statistical techniques to compute the probabilities that the phases have a particular value. It is possible to deduce relations between some structure factors and sums (and sums of squares) of others, which have the effect of constraining the phases to particular values (with high probability, so long as the structure factors are large). For example, the **Sayre probability relation** has the form

$$\text{sign of } F_{h+h',k+k',l+l'} \text{ is probably equal to } (\text{sign of } F_{hkl}) \times (\text{sign of } F_{h'k'l'}) \quad (20.11)$$

For example, if F_{122} and F_{232} are both large and negative, then it is highly likely that F_{354} , provided it is large, will be positive.

(f) Structure refinement

In the final stages of the determination of a crystal structure, the parameters describing the structure (atom positions, for instance) are adjusted systematically to give the best fit between the observed intensities and those calculated from the model of the structure deduced from the diffraction pattern. This process is called **structure refinement**. Not only does the procedure give accurate positions for all the atoms in the unit cell, but it also gives an estimate of the errors in those positions and in the bond lengths and angles derived from them. The procedure also provides information on the vibrational amplitudes of the atoms.



IMPACT ON BIOCHEMISTRY

120.1 X-ray crystallography of biological macromolecules

X-ray crystallography is the deployment of X-ray diffraction techniques for the determination of the location of all the atoms in molecules as complicated as biopolymers. Bragg's law helps us understand the features of one of the most seminal X-ray images of all time, the characteristic X-shaped pattern obtained by Rosalind Franklin and Maurice Wilkins from strands of DNA and used by James Watson and Francis Crick in their construction of the double-helix model of DNA (Fig. 20.26). To interpret this image by using the Bragg law we have to be aware that it was obtained by using a fibre consisting of many DNA molecules oriented with their axes parallel to the axis of the fibre, with X-rays incident from a perpendicular direction. All the molecules in the fibre are parallel (or nearly so), but are randomly distributed in the perpendicular directions; as a result, the diffraction pattern exhibits the periodic structure parallel to the fibre axis superimposed on a general background of scattering from the distribution of molecules in the perpendicular directions.

There are two principal features in Fig. 20.26: the strong 'meridional' scattering upward and downward by the fibre and the X-shaped distribution at smaller scattering angles. Because scattering through large angles occurs for closely spaced features (from $\lambda = 2d \sin \theta$, if d is small, then θ must be large to preserve the equality), we can infer that the meridional scattering arises from closely spaced components and that the inner X-shaped pattern arises from features with a longer periodicity. Because the meridional pattern occurs at a distance of about 10 times that of the innermost spots of the X-pattern, the large-scale structure is about 10 times bigger than the small-scale structure. From the geometry of the instrument, the wavelength of the radiation, and Bragg's law, we can infer that the periodicity of the small-scale feature is 340 pm whereas that of the large-scale feature is 3400 pm (that is, 3.4 nm).

To see that the cross is characteristic of a helix, look at Fig. 20.27. Each turn of the helix defines two planes, one orientated at an angle α to the horizontal and the other at $-\alpha$. As a result, to a first approximation, a helix can be thought of as consisting of an array of planes at an angle α together with an array of planes at an angle $-\alpha$ with a separation within each set determined by the pitch of the helix. Thus, a DNA molecule is like two arrays of planes, each set corresponding to those treated in the derivation of Bragg's law, with a perpendicular separation $d = p \cos \alpha$, where p is the pitch of the helix, each canted at the angles $\pm\alpha$ to the horizontal. The diffraction spots from one set of planes therefore occur at an angle α to the vertical, giving one leg of the X, and those of the other set occur at an angle $-\alpha$, giving rise to the other leg of the X. The

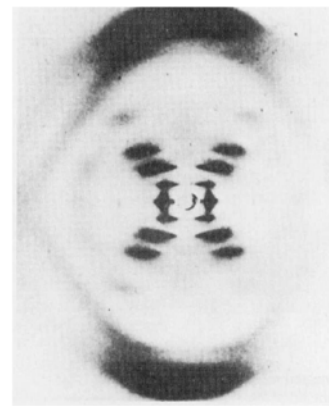


Fig. 20.26 The X-ray diffraction pattern obtained from a fibre of B-DNA. The black dots are the reflections, the points of maximum constructive interference, that are used to determine the structure of the molecule. (Adapted from an illustration that appears in J.P. Glusker and K.N. Trueblood, *Crystal structure analysis: A primer*. Oxford University Press (1972).)

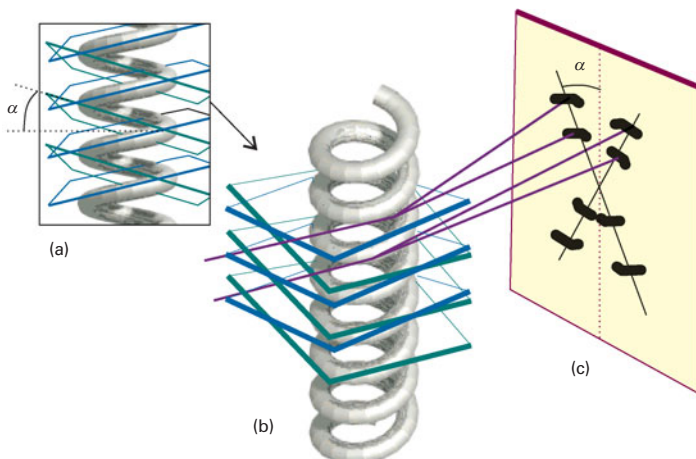
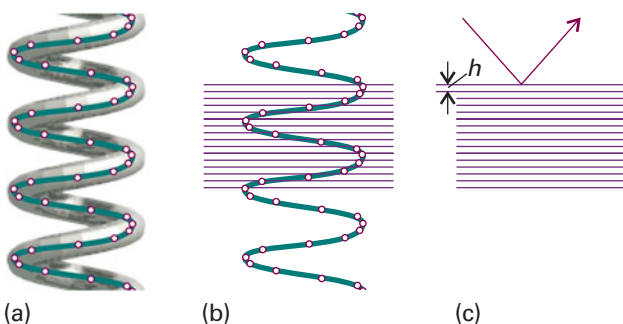


Fig. 20.27 The origin of the X pattern characteristic of diffraction by a helix. (a) A helix can be thought of as consisting of an array of planes at an angle α together with an array of planes at an angle $-\alpha$. (b) The diffraction spots from one set of planes appear at an angle α to the vertical, giving one leg of the X, and those of the other set appear at an angle $-\alpha$, giving rise to the other leg of the X. The lower half of the X appears because the helix has up-down symmetry in this arrangement. (c) The sequence of spots outward along a leg of the X corresponds to first-, second-, ... order diffraction ($n = 1, 2, \dots$).

Fig. 20.28 The effect of the internal structure of the helix on the X-ray diffraction pattern. (a) The residues of the macromolecule are represented by points. (b) Parallel planes passing through the residues are perpendicular to the axis of the molecule. (c) The planes give rise to strong diffraction with an angle that allows us to determine the layer spacing h from $\lambda = 2h \sin \theta$.



experimental arrangement has up–down symmetry, so the diffraction pattern repeats to produce the lower half of the X. The sequence of spots outward along a leg corresponds to first-, second-, . . . order diffraction ($n = 1, 2, \dots$ in eqn 20.4). Therefore from the X-ray pattern, we see at once that the molecule is helical and we can measure the angle α directly, and find $\alpha = 40^\circ$. Finally, with the angle α and the pitch p determined, we can determine the radius r of the helix from $\tan \alpha = p/4r$, from which it follows that $r = (3.4 \text{ nm})/(4 \tan 40^\circ) = 1.0 \text{ nm}$.

To derive the relation between the helix and the cross-like pattern we have ignored the detailed structure of the helix, the fact that it is a periodic array of nucleotide bases, not a smooth wire. In Fig. 20.28 we represent the bases by points, and see that there is an additional periodicity of separation h , forming planes that are perpendicular to the axis to the molecule (and the fibre). These planes give rise to the strong meridional diffraction with an angle that allows us to determine the layer spacing from Bragg's law in the form $\lambda = 2h \sin \theta$ as $h = 340 \text{ pm}$.

The success of modern biochemistry in explaining such processes as DNA replication, protein biosynthesis, and enzyme catalysis is a direct result of developments in preparatory, instrumental, and computational procedures that have led to the determination of large numbers of structures of biological macromolecules by techniques based on X-ray diffraction. Most work is now done not on fibres but on crystals, in which the large molecules lie in orderly ranks. A technique that works well for charged proteins consists of adding large amounts of a salt, such as $(\text{NH}_4)_2\text{SO}_4$, to a buffer solution containing the biopolymer. The increase in the ionic strength of the solution decreases the solubility of the protein to such an extent that the protein precipitates, sometimes as crystals that are amenable to analysis by X-ray diffraction. Other common strategies for inducing crystallization involve the gradual removal of solvent from a biopolymer solution, either by *dialysis* (Impact 15.2) or *vapour diffusion*. In one implementation of the vapour diffusion method, a single drop of biopolymer solution hangs above an aqueous solution (the reservoir), as shown in Fig. 20.29. If the reservoir solution is more concentrated in a non-volatile solute (for example, a salt) than is the biopolymer solution, then solvent will evaporate slowly from the drop until the vapour pressure of water in the closed container reaches a constant, equilibrium value. At the same time, the concentration of biopolymer in the drop increases gradually until crystals begin to form.

Special techniques are used to crystallize hydrophobic proteins, such as those spanning the bilayer of a cell membrane. In such cases, surfactant molecules, which like phospholipids contain polar head groups and hydrophobic tails, are used to encase the protein molecules and make them soluble in aqueous buffer solutions. Dialysis or vapour diffusion may then be used to induce crystallization.

After suitable crystals are obtained, X-ray diffraction data are collected and analysed as described in the previous sections. The three-dimensional structures of a very

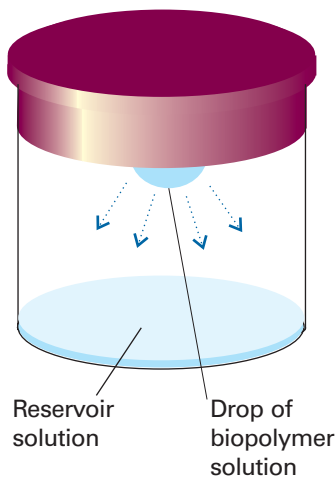


Fig. 20.29 In a common implementation of the vapour diffusion method of biopolymer crystallization, a single drop of biopolymer solution hangs above a reservoir solution that is very concentrated in a non-volatile solute. Solvent evaporates from the more dilute drop until the vapour pressure of water in the closed container reaches a constant equilibrium value. In the course of evaporation (denoted by the downward arrows), the biopolymer solution becomes more concentrated and, at some point, crystals may form.

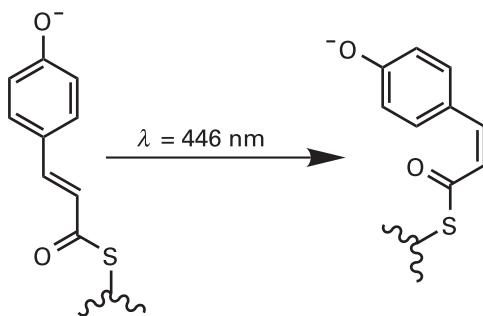


Fig. 20.30 Light-induced isomerization of a protein-bound phenolate ion in the photoactive yellow protein of the bacterium *Ectothiorhodospira halophila*.

large number of biological polymers have been determined in this way. However, the techniques discussed so far give only static pictures and are not useful in studies of dynamics and reactivity. This limitation stems from the fact that the Bragg rotation method requires stable crystals that do not change structure during the lengthy data acquisition times required. However, special time-resolved X-ray diffraction techniques have become available in recent years and it is now possible to make exquisitely detailed measurements of atomic motions during chemical and biochemical reactions.

Time-resolved X-ray diffraction techniques make use of synchrotron sources, which can emit intense polychromatic pulses of X-ray radiation with pulse widths varying from 100 ps to 200 ps ($1 \text{ ps} = 10^{-12} \text{ s}$). Instead of the Bragg method, the Laue method is used because many reflections can be collected simultaneously, rotation of the sample is not required, and data acquisition times are short. However, good diffraction data cannot be obtained from a single X-ray pulse and reflections from several pulses must be averaged together. In practice, this averaging dictates the time resolution of the experiment, which is commonly tens of microseconds or less.

An example of the power of time-resolved X-ray crystallography is the elucidation of structural changes that accompany the activation by light of the photoactive yellow protein of the bacterium *Ectothiorhodospira halophila*. Within 1 ns after absorption of a photon of 446 nm light, a protein-bound phenolate ion undergoes *trans–cis* isomerization to form the intermediate shown in Fig. 20.30. A series of rearrangements then follows, which includes the ejection of the ion from its binding site deep in the protein, its return to the site, and re-formation of the *cis* conformation. The physiological outcome of this cycle is a *negative phototactic response*, or movement of the organism away from light. Time-resolved X-ray diffraction studies in the nanosecond to millisecond ranges identified a number of structural changes that follow electronic excitation of the phenolate ion with a laser pulse: isomerization, ejection, protonation of the exposed ion, and a number of amino acid motions.

20.4 Neutron and electron diffraction

According to the de Broglie relation (eqn 8.12, $\lambda = h/p$), particles have wavelengths and may therefore undergo diffraction. Neutrons generated in a nuclear reactor and then slowed to thermal velocities have wavelengths similar to those of X-rays and may also be used for diffraction studies. For instance, a neutron generated in a reactor and slowed to thermal velocities by repeated collisions with a moderator (such as graphite) until it is travelling at about 4 km s^{-1} has a wavelength of about 100 pm. In practice, a range of wavelengths occurs in a neutron beam, but a monochromatic beam can be selected by diffraction from a crystal, such as a single crystal of germanium.

Comment 20.3

The text's web site contains links to databases of structures of biological macromolecules.

Example 20.5 Calculating the typical wavelength of thermal neutrons

Calculate the typical wavelength of neutrons that have reached thermal equilibrium with their surroundings at 373 K.

Method We need to relate the wavelength to the temperature. There are two linking steps. First, the de Broglie relation expresses the wavelength in terms of the linear momentum. Then the linear momentum can be expressed in terms of the kinetic energy, the mean value of which is given in terms of the temperature by the equipartition theorem (see Section 17.3).

Answer From the equipartition principle, we know that the mean translational kinetic energy of a neutron at a temperature T travelling in the x -direction is $E_K = \frac{1}{2}kT$. The kinetic energy is also equal to $p^2/2m$, where p is the momentum of the neutron and m is its mass. Hence, $p = (mkT)^{1/2}$. It follows from the de Broglie relation $\lambda = h/p$ that the neutron's wavelength is

$$\lambda = \frac{h}{(mkT)^{1/2}}$$

Therefore, at 373 K,

$$\begin{aligned}\lambda &= \frac{6.626 \times 10^{-34} \text{ J s}}{\{(1.675 \times 10^{-27} \text{ kg}) \times (1.381 \times 10^{-23} \text{ J K}^{-1}) \times (373 \text{ K})\}^{1/2}} \\ &= \frac{6.626 \times 10^{-34} \text{ J s}}{(1.675 \times 1.381 \times 373 \times 10^{-50})^{1/2} \cdot (\text{kg}^2 \text{ m}^2 \text{ s}^{-2})^{1/2}} \\ &= 2.26 \times 10^{-10} \text{ m} = 226 \text{ pm}\end{aligned}$$

where we have used $1 \text{ J} = 1 \text{ kg m}^2 \text{ s}^{-2}$.

Self-test 20.6 Calculate the temperature needed for the average wavelength of the neutrons to be 100 pm. [$1.90 \times 10^3 \text{ K}$]

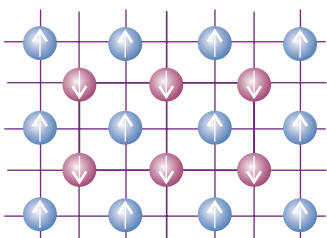


Fig. 20.31 If the spins of atoms at lattice points are orderly, as in this material, where the spins of one set of atoms are aligned antiparallel to those of the other set, neutron diffraction detects two interpenetrating simple cubic lattices on account of the magnetic interaction of the neutron with the atoms, but X-ray diffraction would see only a single bcc lattice.

Neutron diffraction differs from X-ray diffraction in two main respects. First, the scattering of neutrons is a nuclear phenomenon. Neutrons pass through the extra-nuclear electrons of atoms and interact with the nuclei through the ‘strong force’ that is responsible for binding nucleons together. As a result, the intensity with which neutrons are scattered is independent of the number of electrons and neighbouring elements in the periodic table may scatter neutrons with markedly different intensities. Neutron diffraction can be used to distinguish atoms of elements such as Ni and Co that are present in the same compound and to study order-disorder phase transitions in FeCo. A second difference is that neutrons possess a magnetic moment due to their spin. This magnetic moment can couple to the magnetic fields of atoms or ions in a crystal (if the ions have unpaired electrons) and modify the diffraction pattern. One consequence is that neutron diffraction is well suited to the investigation of magnetically ordered lattices in which neighbouring atoms may be of the same element but have different orientations of their electronic spin (Fig. 20.31).

Electrons accelerated through a potential difference of 40 kV have wavelengths of about 6 pm, and so are also suitable for diffraction studies. However, their main application is to the study of surfaces, and we postpone their discussion until Chapter 25.

Crystal structure

The bonding within a solid may be of various kinds. Simplest of all (in principle) are elemental metals, where electrons are delocalized over arrays of identical cations and bind them together into a rigid but ductile and malleable whole.

20.5 Metallic solids

Most metallic elements crystallize in one of three simple forms, two of which can be explained in terms of hard spheres packing together in the closest possible arrangement.

(a) Close packing

Figure 20.32 shows a **close-packed** layer of identical spheres, one with maximum utilization of space. A close-packed three-dimensional structure is obtained by stacking such close-packed layers on top of one another. However, this stacking can be done in different ways, which result in close-packed **polytypes**, or structures that are identical in two dimensions (the close-packed layers) but differ in the third dimension.

In all polytypes, the spheres of second close-packed layer lie in the depressions of the first layer (Fig. 20.33). The third layer may be added in either of two ways. In one, the spheres are placed so that they reproduce the first layer (Fig. 20.34a), to give an ABA pattern of layers. Alternatively, the spheres may be placed over the gaps in the first layer (Fig. 20.34b), so giving an ABC pattern. Two polytypes are formed if the two stacking patterns are repeated in the vertical direction. If the ABA pattern is repeated, to give the sequence of layers ABABAB . . . , the spheres are **hexagonally close-packed**

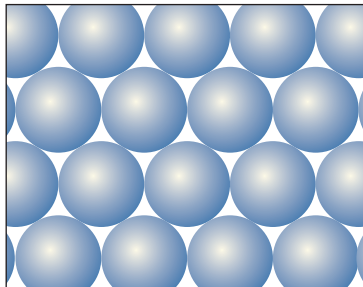


Fig. 20.32 The first layer of close-packed spheres used to build a three-dimensional close-packed structure.

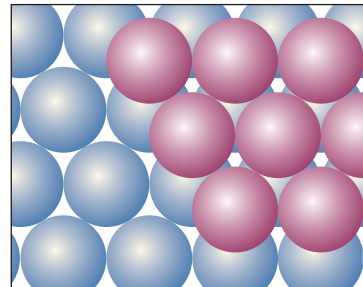
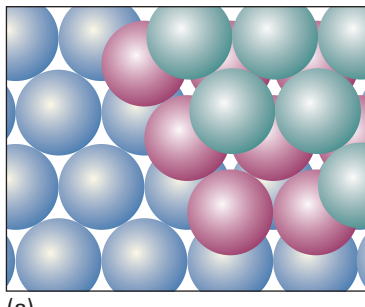
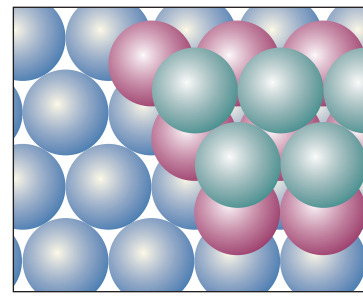


Fig. 20.33 The second layer of close-packed spheres occupies the dips of the first layer. The two layers are the AB component of the close-packed structure.



(a)



(b)

Fig. 20.34 (a) The third layer of close-packed spheres might occupy the dips lying directly above the spheres in the first layer, resulting in an ABA structure, which corresponds to hexagonal close-packing. (b) Alternatively, the third layer might lie in the dips that are not above the spheres in the first layer, resulting in an ABC structure, which corresponds to cubic close-packing

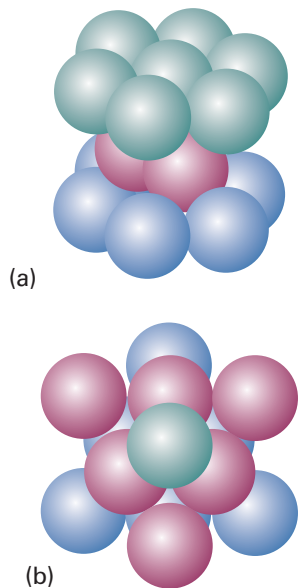


Fig. 20.35 A fragment of the structure shown in Fig. 20.34 revealing the (a) hexagonal (b) cubic symmetry. The tints on the spheres are the same as for the layers in Fig. 20.34.

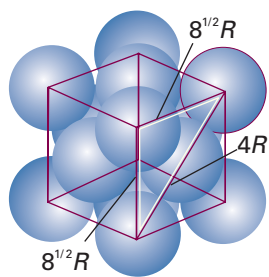


Fig. 20.36 The calculation of the packing fraction of a ccp unit cell.

Table 20.2 The crystal structures of some elements

Structure	Element
hcp*	Be, Cd, Co, He, Mg, Sc, Ti, Zn
fcc* (ccp, cubic F)	Ag, Al, Ar, Au, Ca, Cu, Kr, Ne, Ni, Pd, Pb, Pt, Rh, Rn, Sr, Xe
bcc (cubic I)	Ba, Cs, Cr, Fe, K, Li, Mn, Mo, Rb, Na, Ta, W, V
cubic P	Po

* Close-packed structures.

(hcp). Alternatively, if the ABC pattern is repeated, to give the sequence ABCABC . . . , the spheres are **cubic close-packed** (ccp). We can see the origins of these names by referring to Fig. 20.35. The ccp structure gives rise to a face-centred unit cell, so may also be denoted cubic F (or fcc, for face-centred cubic).² It is also possible to have random sequences of layers; however, the hcp and ccp polytypes are the most important. Table 20.2 lists some elements possessing these structures.

The compactness of close-packed structures is indicated by their **coordination number**, the number of atoms immediately surrounding any selected atom, which is 12 in all cases. Another measure of their compactness is the **packing fraction**, the fraction of space occupied by the spheres, which is 0.740 (see the following *Justification*). That is, in a close-packed solid of identical hard spheres, only 26.0 per cent of the volume is empty space. The fact that many metals are close-packed accounts for their high densities.

Justification 20.3 The packing fraction

To calculate a packing fraction of a ccp structure, we first calculate the volume of a unit cell, and then calculate the total volume of the spheres that fully or partially occupy it. The first part of the calculation is a straightforward exercise in geometry. The second part involves counting the fraction of spheres that occupy the cell.

Refer to Fig. 20.36. Because a diagonal of any face passes completely through one sphere and halfway through two other spheres, its length is $4R$. The length of a side is therefore $8^{1/2}R$ and the volume of the unit cell is $8^{3/2}R^3$. Because each cell contains the equivalent of $6 \times \frac{1}{2} + 8 \times \frac{1}{8} = 4$ spheres, and the volume of each sphere is $\frac{4}{3}\pi R^3$, the total occupied volume is $\frac{16}{3}\pi R^3$. The fraction of space occupied is therefore $\frac{16}{3}\pi R^3 / 8^{3/2}R^3 = \frac{16}{3}\pi / 8^{3/2}$, or 0.740. Because an hcp structure has the same coordination number, its packing fraction is the same. The packing fractions of structures that are not close-packed are calculated similarly (see Exercises 20.14 and 20.17 and Problem 20.24).

(b) Less closely packed structures

As shown in Table 20.2, a number of common metals adopt structures that are less than close-packed. The departure from close packing suggests that factors such as specific covalent bonding between neighbouring atoms are beginning to influence the structure and impose a specific geometrical arrangement. One such arrangement results in a cubic I (bcc, for body-centred cubic) structure, with one sphere at the centre of a cube formed by eight others. The coordination number of a bcc structure is

² Strictly speaking, ccp refers to a close-packed arrangement whereas fcc refers to the lattice type of the common representation of ccp. However, this distinction is rarely made.

only 8, but there are six more atoms not much further away than the eight nearest neighbours. The packing fraction of 0.68 is not much smaller than the value for a close-packed structure (0.74), and shows that about two-thirds of the available space is actually occupied.

20.6 Ionic solids

Two questions arise when we consider ionic solids: the relative locations adopted by the ions and the energetics of the resulting structure.

(a) Structure

When crystals of compounds of monatomic ions (such as NaCl and MgO) are modelled by stacks of hard spheres it is essential to allow for the different ionic radii (typically with the cations smaller than the anions) and different charges. The **coordination number** of an ion is the number of nearest neighbours of opposite charge; the structure itself is characterized as having (n_+, n_-) **coordination**, where n_+ is the coordination number of the cation and n_- that of the anion.

Even if, by chance, the ions have the same size, the problems of ensuring that the unit cells are electrically neutral makes it impossible to achieve 12-coordinate close-packed ionic structures. As a result, ionic solids are generally less dense than metals. The best packing that can be achieved is the (8,8)-coordinate **caesium-chloride structure** in which each cation is surrounded by eight anions and each anion is surrounded by eight cations (Fig. 20.37). In this structure, an ion of one charge occupies the centre of a cubic unit cell with eight counter ions at its corners. The structure is adopted by CsCl itself and also by CaS, CsCN (with some distortion), and CuZn.

When the radii of the ions differ more than in CsCl, even eight-coordinate packing cannot be achieved. One common structure adopted is the (6,6)-coordinate **rock-salt structure** typified by NaCl (Fig. 20.38). In this structure, each cation is surrounded by six anions and each anion is surrounded by six cations. The rock-salt structure can be pictured as consisting of two interpenetrating slightly expanded cubic F (fcc) arrays, one composed of cations and the other of anions. This structure is adopted by NaCl itself and also by several other MX compounds, including KBr, AgCl, MgO, and ScN.

The switch from the caesium-chloride structure to the rock-salt structure is related to the value of the **radius ratio**, γ :

$$\gamma = \frac{r_{\text{smaller}}}{r_{\text{larger}}} \quad [20.12]$$

The two radii are those of the larger and smaller ions in the crystal. The **radius-ratio rule** states that the caesium-chloride structure should be expected when $\gamma > 3^{1/2} - 1 = 0.732$ and that the rock-salt structure should be expected when $2^{1/2} - 1 = 0.414 < \gamma < 0.732$. For $\gamma < 0.414$, the most efficient packing leads to four-coordination of the type exhibited by the sphalerite (or zinc blende) form of ZnS (Fig. 20.39). The rule is derived by considering the geometrical problem of packing the maximum number of hard spheres of one radius around a hard sphere of a different radius. The deviation of a structure from that expected on the basis of the radius-ratio rule is often taken to be an indication of a shift from ionic towards covalent bonding; however, a major source of unreliability is the arbitrariness of ionic radii and their variation with coordination number.

Ionic radii are derived from the distance between centres of adjacent ions in a crystal. However, we need to apportion the total distance between the two ions by defining the radius of one ion and then inferring the radius of the other ion. One scale that is widely used is based on the value 140 pm for the radius of the O²⁻ ion (Table 20.3).

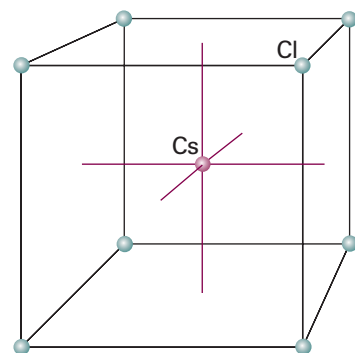


Fig. 20.37 The caesium-chloride structure consists of two interpenetrating simple cubic arrays of ions, one of cations and the other of anions, so that each cube of ions of one kind has a counter-ion at its centre.

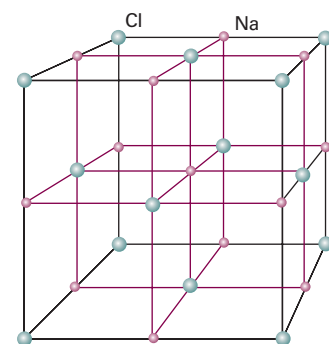


Fig. 20.38 The rock-salt (NaCl) structure consists of two mutually interpenetrating slightly expanded face-centred cubic arrays of ions. The entire assembly shown here is the unit cell.

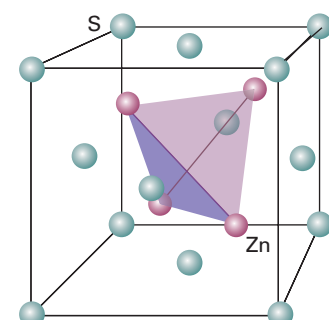


Fig. 20.39 The structure of the sphalerite form of ZnS showing the location of the Zn atoms in the tetrahedral holes formed by the array of S atoms. (There is an S atom at the centre of the cube inside the tetrahedron of Zn atoms.)

Synoptic table 20.3* Ionic radii, r/pm

Na^+	102(6†), 116(8)
K^+	138(6), 151(8)
F^-	128(2), 131(4)
Cl^-	181 (close packing)

* More values are given in the *Data section*.

† Coordination number.

Other scales are also available (such as one based on F^- for discussing halides), and it is essential not to mix values from different scales. Because ionic radii are so arbitrary, predictions based on them must be viewed cautiously.

(b) Energetics

The **lattice energy** of a solid is the difference in potential energy of the ions packed together in a solid and widely separated as a gas. The lattice energy is always positive; a high lattice energy indicates that the ions interact strongly with one another to give a tightly bonded solid. The **lattice enthalpy**, ΔH_L , is the change in standard molar enthalpy for the process



and its equivalent for other charge types and stoichiometries. The lattice enthalpy is equal to the lattice energy at $T = 0$; at normal temperatures they differ by only a few kilojoules per mole, and the difference is normally neglected.

Each ion in a solid experiences electrostatic attractions from all the other oppositely charged ions and repulsions from all the other like-charged ions. The total Coulombic potential energy is the sum of all the electrostatic contributions. Each cation is surrounded by anions, and there is a large negative contribution from the attraction of the opposite charges. Beyond those nearest neighbours, there are cations that contribute a positive term to the total potential energy of the central cation. There is also a negative contribution from the anions beyond those cations, a positive contribution from the cations beyond them, and so on to the edge of the solid. These repulsions and attractions become progressively weaker as the distance from the central ion increases, but the net outcome of all these contributions is a lowering of energy.

First, consider a simple one-dimensional model of a solid consisting of a long line of uniformly spaced alternating cations and anions, with d the distance between their centres, the sum of the ionic radii (Fig. 20.40). If the charge numbers of the ions have the same absolute value (+1 and -1, or +2 and -2, for instance), then $z_1 = +z$, $z_2 = -z$, and $z_1 z_2 = -z^2$. The potential energy of the central ion is calculated by summing all the terms, with negative terms representing attractions to oppositely charged ions and positive terms representing repulsions from like-charged ions. For the interaction with ions extending in a line to the right of the central ion, the lattice energy is

$$\begin{aligned} E_P &= \frac{1}{4\pi\epsilon_0} \times \left(-\frac{z^2 e^2}{d} + \frac{z^2 e^2}{2d} - \frac{z^2 e^2}{3d} + \frac{z^2 e^2}{4d} - \dots \right) \\ &= -\frac{z^2 e^2}{4\pi\epsilon_0 d} \left(1 - \frac{1}{2} + \frac{1}{3} - \frac{1}{4} + \dots \right) \\ &= -\frac{z^2 e^2}{4\pi\epsilon_0 d} \times \ln 2 \end{aligned}$$

We have used the relation $1 - \frac{1}{2} + \frac{1}{3} - \frac{1}{4} + \dots = \ln 2$. Finally, we multiply E_P by 2 to obtain the total energy arising from interactions on each side of the ion and then multiply by Avogadro's constant, N_A , to obtain an expression for the lattice energy per mole of ions. The outcome is

$$E_P = -2 \ln 2 \times \frac{z^2 N_A e^2}{4\pi\epsilon_0 d}$$

with $d = r_{\text{cation}} + r_{\text{anion}}$. This energy is negative, corresponding to a net attraction. The calculation we have just performed can be extended to three-dimensional arrays of ions with different charges:

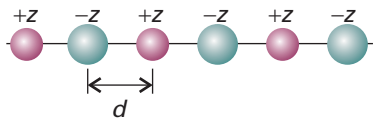


Fig. 20.40 A line of alternating cations and ions used in the calculation of the Madelung constant in one dimension.

$$E_p = -A \times \frac{|z_1 z_2| N_A e^2}{4\pi \epsilon_0 d} \quad (20.13)$$

The factor A is a positive numerical constant called the **Madelung constant**; its value depends on how the ions are arranged about one another. For ions arranged in the same way as in sodium chloride, $A = 1.748$. Table 20.4 lists Madelung constants for other common structures.

There are also repulsions arising from the overlap of the atomic orbitals of the ions and the role of the Pauli principle. These repulsions are taken into account by supposing that, because wavefunctions decay exponentially with distance at large distances from the nucleus, and repulsive interactions depend on the overlap of orbitals, the repulsive contribution to the potential energy has the form

$$E_p^* = N_A C' e^{-d/d^*} \quad (20.14)$$

with C' and d^* constants; the latter is commonly taken to be 34.5 pm. The total potential energy is the sum of E_p and E_p^* , and passes through a minimum when $d(E_p + E_p^*)/dd = 0$ (Fig. 20.41). A short calculation leads to the following expression for the minimum total potential energy (see Exercise 20.21a):

$$E_{p,\min} = -\frac{N_A |z_A z_B| e^2}{4\pi \epsilon_0 d} \left(1 - \frac{d^*}{d} \right) A \quad (20.15)$$

This expression is called the **Born–Mayer equation**. Provided we ignore zero-point contributions to the energy, we can identify the negative of this potential energy with the lattice energy. We see that large lattice energies are expected when the ions are highly charged (so $|z_A z_B|$ is large) and small (so d is small).

Experimental values of the lattice enthalpy (the enthalpy, rather than the energy) are obtained by using a **Born–Haber cycle**, a closed path of transformations starting and ending at the same point, one step of which is the formation of the solid compound from a gas of widely separated ions. A typical cycle, for potassium chloride, is shown in Fig. 20.42. It consists of the following steps (for convenience, starting at the elements):

	$\Delta H/\text{kJ mol}^{-1}$
1. Sublimation of K(s)	+89 [dissociation enthalpy of K(s)]
2. Dissociation of $\frac{1}{2} \text{Cl}_2(\text{g})$	+122 [$\frac{1}{2} \times$ dissociation enthalpy of $\text{Cl}_2(\text{g})$]
3. Ionization of K(g)	+418 [ionization enthalpy of K(g)]
4. Electron attachment to Cl(g)	-349 [electron gain enthalpy of Cl(g)]
5. Formation of solid from gas	$-\Delta H_L/\text{(kJ mol}^{-1}\text{)}$
6. Decomposition of compound	+437 [negative of enthalpy of formation of $\text{KCl}(\text{s})$]

Because the sum of these enthalpy changes is equal to zero, we can infer from

$$89 + 122 + 418 - 349 - \Delta H_L/\text{(kJ mol}^{-1}\text{)} + 437 = 0$$

that $\Delta H_L = +717 \text{ kJ mol}^{-1}$. Some lattice enthalpies obtained in this way are listed in Table 20.5. As can be seen from the data, the trends in values are in general accord with the predictions of the Born–Mayer equation. Agreement is typically taken to imply that the ionic model of bonding is valid for the substance; disagreement implies that there is a covalent contribution to the bonding.

Table 20.4 Madelung constants

Structural type*	A
Caesium chloride	1.763
Fluorite	2.519
Rock salt	1.748
Rutile	2.408
Sphalerite	1.638
Wurtzite	1.641

* For descriptions of the structural types not covered in this chapter, see references in *Further reading*.

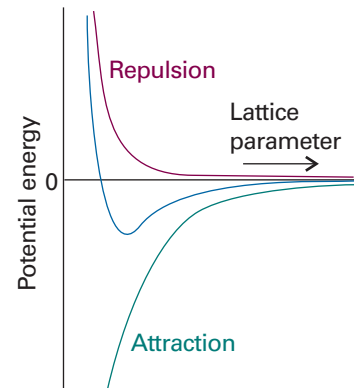


Fig. 20.41 The contributions to the total potential energy of an ionic crystal.

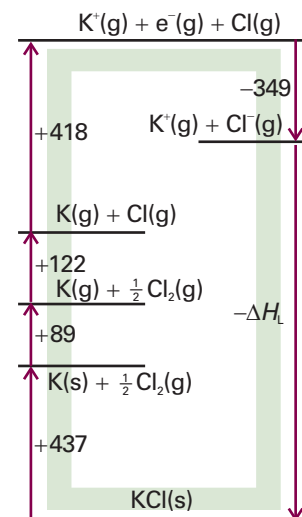


Fig. 20.42 The Born–Haber cycle for KCl at 298 K. Enthalpies changes are in kilojoules per mole.

Synoptic table 20.5* Lattice enthalpies at 298 K, $\Delta H_L/(kJ\ mol^{-1})$

NaF	787
NaBr	751
MgO	3850
MgS	3406

* More values are given in the *Data section*.

Comment 20.4

Allotropes are distinct forms of an element that differ in the way that atoms are linked. For example, oxygen has two allotropes: O_2 and O_3 (ozone).

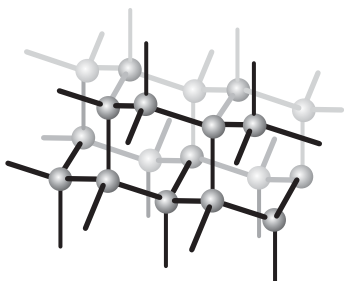


Fig. 20.43 A fragment of the structure of diamond. Each C atom is tetrahedrally bonded to four neighbours. This framework-like structure results in a rigid crystal.

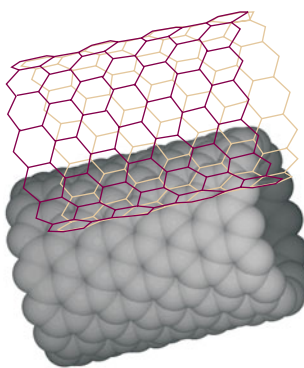


Fig. 20.45 In a single-walled nanotube (SWNT), sp^2 -hybridized carbon atoms form hexagonal rings that grow as tubes with diameters between 1 and 2 nm and lengths of several micrometres.

20.7 Molecular solids and covalent networks

X-ray diffraction studies of solids reveal a huge amount of information, including interatomic distances, bond angles, stereochemistry, and vibrational parameters. In this section we can do no more than hint at the diversity of types of solids found when molecules pack together or atoms link together in extended networks.

In **covalent network solids**, covalent bonds in a definite spatial orientation link the atoms in a network extending through the crystal. The demands of directional bonding, which have only a small effect on the structures of many metals, now override the geometrical problem of packing spheres together, and elaborate and extensive structures may be formed. Examples include silicon, red phosphorus, boron nitride, and—very importantly—diamond, graphite, and carbon nanotubes, which we discuss in detail.

Diamond and graphite are two allotropes of carbon. In diamond each sp^3 -hybridized carbon is bonded tetrahedrally to its four neighbours (Fig. 20.43). The network of strong C–C bonds is repeated throughout the crystal and, as a result, diamond is the hardest known substance.

In graphite, σ bonds between sp^2 -hybridized carbon atoms form hexagonal rings which, when repeated throughout a plane, give rise to sheets (Fig. 20.44). Because the sheets can slide against each other when impurities are present, graphite is used widely as a lubricant.

Carbon nanotubes are thin cylinders of carbon atoms that are both mechanically strong and highly conducting (see *Impact I20.2*). They are synthesized by condensing a carbon plasma either in the presence or absence of a catalyst. The simplest structural motif is called a *single-walled nanotube* (SWNT) and is shown in Fig. 20.45. In a SWNT, sp^2 -hybridized carbon atoms form hexagonal rings reminiscent of the structure of the carbon sheets found in graphite. The tubes have diameters between 1 and 2 nm and lengths of several micrometres. The features shown in Fig. 20.45 have been confirmed by direct visualization with scanning tunnelling microscopy (*Impact I9.1*). A *multi-walled nanotube* (MWNT) consists of several concentric SWNTs and its diameter varies between 2 and 25 nm.

Molecular solids, which are the subject of the overwhelming majority of modern structural determinations, are held together by van der Waals interactions (Chapter 18). The observed crystal structure is Nature's solution to the problem of condensing objects of various shapes into an aggregate of minimum energy (actually, for $T > 0$, of

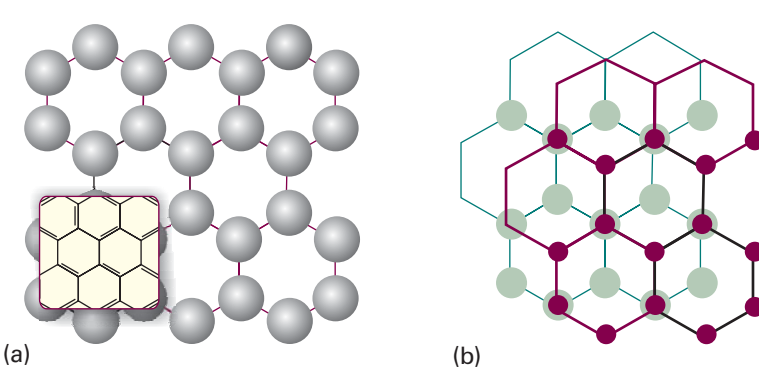


Fig. 20.44 Graphite consists of flat planes of hexagons of carbon atoms lying above one another. (a) The arrangement of carbon atoms in a sheet; (b) the relative arrangement of neighbouring sheets. When impurities are present, the planes can slide over one another easily.

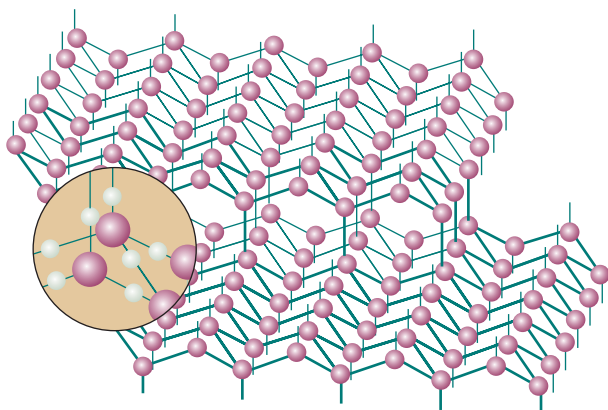


Fig. 20.46 A fragment of the crystal structure of ice (ice-I). Each O atom is at the centre of a tetrahedron of four O atoms at a distance of 276 pm. The central O atom is attached by two short O—H bonds to two H atoms and by two long hydrogen bonds to the H atoms of two of the neighbouring molecules. Overall, the structure consists of planes of hexagonal puckered rings of H_2O molecules (like the chair form of cyclohexane).

minimum Gibbs energy). The prediction of the structure is a very difficult task, but software specifically designed to explore interaction energies can now make reasonably reliable predictions. The problem is made more complicated by the role of hydrogen bonds, which in some cases dominate the crystal structure, as in ice (Fig. 20.46), but in others (for example, in phenol) distort a structure that is determined largely by the van der Waals interactions.

The properties of solids

In this section we consider how the bulk properties of solids, particularly their mechanical, electrical, optical, and magnetic properties, stem from the properties of their constituent atoms. The rational fabrication of modern materials depends crucially on an understanding of this link.

20.8 Mechanical properties

The fundamental concepts for the discussion of the mechanical properties of solids are stress and strain. The **stress** on an object is the applied force divided by the area to which it is applied. The **strain** is the resulting distortion of the sample. The general field of the relations between stress and strain is called **rheology**.

Stress may be applied in a number of different ways. Thus, **uniaxial stress** is a simple compression or extension in one direction (Fig. 20.47); **hydrostatic stress** is a stress applied simultaneously in all directions, as in a body immersed in a fluid. A **pure shear** is a stress that tends to push opposite faces of the sample in opposite directions. A sample subjected to a small stress typically undergoes **elastic deformation** in the sense that it recovers its original shape when the stress is removed. For low stresses, the strain is linearly proportional to the stress. The response becomes nonlinear at high stresses but may remain elastic. Above a certain threshold, the strain becomes **plastic** in the sense that recovery does not occur when the stress is removed. Plastic deformation occurs when bond breaking takes place and, in pure metals, typically takes place through the agency of dislocations. Brittle solids, such as ionic solids, exhibit sudden fracture as the stress focused by cracks causes them to spread catastrophically.

The response of a solid to an applied stress is commonly summarized by a number of coefficients of proportionality known as ‘moduli’:

Comment 20.5

The web site contains links to databases of properties of materials, such as metals and polymers.

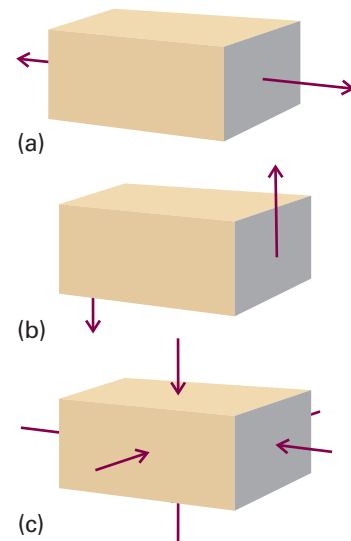


Fig. 20.47 Types of stress applied to a body.
(a) Uniaxial stress, (b) shear stress,
(c) hydrostatic pressure.

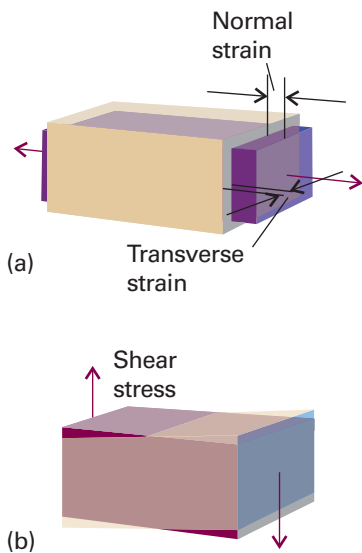


Fig. 20.48 (a) Normal stress and the resulting strain. (b) Shear stress. Poisson's ratio indicates the extent to which a body changes shape when subjected to a uniaxial stress.

$$\text{Young's modulus: } E = \frac{\text{normal stress}}{\text{normal strain}} \quad [20.16a]$$

$$\text{Bulk modulus: } K = \frac{\text{pressure}}{\text{fractional change in volume}} \quad [20.16b]$$

$$\text{Shear modulus: } G = \frac{\text{shear stress}}{\text{shear strain}} \quad [20.16c]$$

where 'normal stress' refers to stretching and compression of the material, as shown in Fig. 20.48a and 'shear stress' refers to the stress depicted in Fig. 20.48b. The bulk modulus is the inverse of the isothermal compressibility, κ , first encountered in Section 2.11 (eqn 2.44, $\kappa = -(\partial V / \partial p)_T / V$). A third ratio indicates how the sample changes its shape:

$$\text{Poisson's ratio: } \nu_p = \frac{\text{transverse strain}}{\text{normal strain}} \quad [20.17]$$

The moduli are interrelated:

$$G = \frac{E}{2(1 + \nu_p)} \quad K = \frac{E}{3(1 - 2\nu_p)} \quad (20.18)$$

We can use thermodynamic arguments to discover the relation of the moduli to the molecular properties of the solid. Thus, in the *Justification* below, we show that, if neighbouring molecules interact by a Lennard-Jones potential, then the bulk modulus and the compressibility of the solid are related to the Lennard-Jones parameter ϵ (the depth of the potential well) by

$$K = \frac{8N_A\epsilon}{V_m} \quad \kappa = \frac{V_m}{8N_A\epsilon} \quad (20.19)$$

We see that the bulk modulus is large (the solid stiff) if the potential well represented by the Lennard-Jones potential is deep and the solid is dense (its molar volume small).

Justification 20.4 The relation between compressibility and molecular interactions

First, we combine the definition of $K = 1/\kappa$, with the thermodynamic relation $p = -(\partial U / \partial V)_T$ (this is eqn 3.45), to obtain

$$K = V \left(\frac{\partial^2 U}{\partial V^2} \right)_T$$

This expression shows that the bulk modulus (and through eqn 20.18, the other two moduli) depends on the curvature of a plot of the internal energy against volume. To develop this conclusion, we note that the variation of internal energy with volume can be expressed in terms of its variation with a lattice parameter, R , such as the length of the side of a unit cell.

$$\frac{\partial U}{\partial V} = \frac{\partial U}{\partial R} \frac{\partial R}{\partial V}$$

and so

$$\frac{\partial^2 U}{\partial V^2} = \frac{\partial U}{\partial R} \frac{\partial^2 R}{\partial V^2} + \frac{\partial^2 U}{\partial V \partial R} \frac{\partial R}{\partial V} = \frac{\partial U}{\partial R} \frac{\partial^2 R}{\partial V^2} + \frac{\partial^2 U}{\partial R^2} \left(\frac{\partial R}{\partial V} \right)^2$$

To calculate K at the equilibrium volume of the sample, we set $R = R_0$ and recognize that $\partial U / \partial R = 0$ at equilibrium, so

$$K = V \left(\frac{\partial^2 U}{\partial R^2} \right)_{T,0} \left(\frac{\partial R}{\partial V} \right)_{T,0}^2$$

where the 0 denotes that the derivatives are evaluated at the equilibrium dimensions of the unit cell by setting $R = R_0$ after the derivative has been calculated. At this point we can write $V = aR^3$, where a is a constant that depends on the crystal structure, which implies that $\partial R/\partial V = 1/(3aR^2)$. Then, if the internal energy is given by a pairwise Lennard-Jones (12,6)-potential, eqn 18.31, we can write

$$\left(\frac{\partial^2 U}{\partial R^2} \right)_{T,0} = \frac{72nN_A\epsilon}{R_0^2} \quad (20.20)$$

where n is the amount of substance in the sample of volume V_0 . It then follows that

$$K = \frac{72nN_A\epsilon}{9aR^3} = \frac{8nN_A\epsilon}{V_0} = \frac{8N_A\epsilon}{V_m}$$

where we have used $V_m = V_0/n$, which is the first of eqn 20.19. Its reciprocal is κ .

The typical behaviour of a solid under stress is illustrated in Fig. 20.49. For small strains, the stress-strain relation is a Hooke's law of force, with the strain directly proportional to the stress. For larger strains, though, dislocations begin to play a major role and the strain becomes plastic in the sense that the sample does not recover its original shape when the stress is removed.

The differing rheological characteristics of metals can be traced to the presence of **slip planes**, which are planes of atoms that under stress may slip or slide relative to one another. The slip planes of a CCP structure are the close-packed planes, and careful inspection of a unit cell shows that there are eight sets of slip planes in different directions. As a result, metals with cubic close-packed structures, like copper, are malleable: they can easily be bent, flattened, or pounded into shape. In contrast, a hexagonal close-packed structure has only one set of slip planes; and metals with hexagonal close packing, like zinc or cadmium, tend to be brittle.

20.9 Electrical properties

We shall confine attention to electronic conductivity, but note that some ionic solids display ionic conductivity. Two types of solid are distinguished by the temperature dependence of their electrical conductivity (Fig. 20.50):

A **metallic conductor** is a substance with a conductivity that decreases as the temperature is raised.

A **semiconductor** is a substance with a conductivity that increases as the temperature is raised.

A semiconductor generally has a lower conductivity than that typical of metals, but the magnitude of the conductivity is not the criterion of the distinction. It is conventional to classify semiconductors with very low electrical conductivities, such as most synthetic polymers, as **insulators**. We shall use this term, but it should be appreciated that it is one of convenience rather than one of fundamental significance. A **superconductor** is a solid that conducts electricity without resistance.

(a) The formation of bands

The central aspect of solids that determines their electrical properties is the distribution of their electrons. There are two models of this distribution. In one, the **nearly**

Comment 20.6

To obtain the result in eqn 20.20, we have used the fact that, at equilibrium, $R = R_0$ and $\sigma^6/R_0^6 = \frac{1}{2}$, where σ is the scale parameter for the intermolecular potential (r_0 in eqn 18.31).

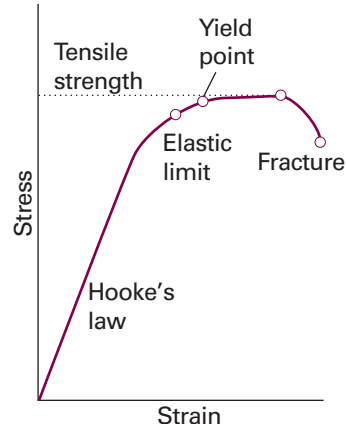


Fig. 20.49 At small strains, a body obeys Hooke's law (stress proportional to strain) and is elastic (recovers its shape when the stress is removed). At high strains, the body is no longer elastic, may yield and become plastic. At even higher strains, the solid fails (at its limiting tensile strength) and finally fractures.

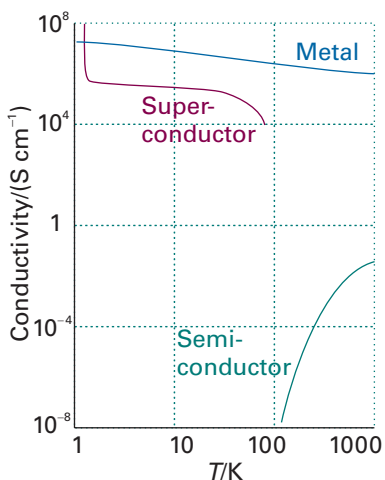


Fig. 20.50 The variation of the electrical conductivity of a substance with temperature is the basis of its classification as a metallic conductor, a semiconductor, or a superconductor. We shall see in Chapter 21 that conductivity is expressed in siemens per metre (S m^{-1} or, as here, S cm^{-1}), where $1 \text{ S} = 1 \Omega^{-1}$ (the resistance is expressed in ohms, Ω).

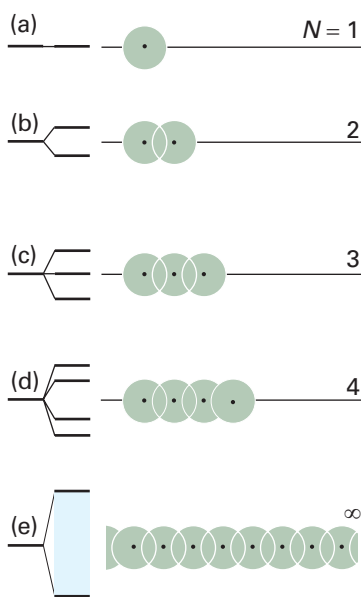


Fig. 20.51 The formation of a band of N molecular orbitals by successive addition of N atoms to a line. Note that the band remains of finite width as N becomes infinite and, although it looks continuous, it consists of N different orbitals.

free-electron approximation, the valence electrons are assumed to be trapped in a box with a periodic potential, with low energy corresponding to the locations of cations. In the **tight-binding approximation**, the valence electrons are assumed to occupy molecular orbitals delocalized throughout the solid. The latter model is more in accord with the discussion in the foregoing chapters, and we confine our attention to it.

We shall consider a one-dimensional solid, which consists of a single, infinitely long line of atoms. At first sight, this model may seem too restrictive and unrealistic. However, not only does it give us the concepts we need to understand conductivity in three-dimensional, macroscopic samples of metals and semiconductors, it is also the starting point for the description of long and thin structures, such as the carbon nanotubes discussed earlier in the chapter.

Suppose that each atom has one s orbital available for forming molecular orbitals. We can construct the LCAO-MOs of the solid by adding N atoms in succession to a line, and then infer the electronic structure using the building-up principle. One atom contributes one s orbital at a certain energy (Fig. 20.51). When a second atom is brought up it overlaps the first and forms bonding and antibonding orbitals. The third atom overlaps its nearest neighbour (and only slightly the next-nearest), and from these three atomic orbitals, three molecular orbitals are formed: one is fully bonding, one fully antibonding, and the intermediate orbital is nonbonding between neighbours. The fourth atom leads to the formation of a fourth molecular orbital. At this stage, we can begin to see that the general effect of bringing up successive atoms is to spread the range of energies covered by the molecular orbitals, and also to fill in the range of energies with more and more orbitals (one more for each atom). When N atoms have been added to the line, there are N molecular orbitals covering a band of energies of finite width, and the Hückel secular determinant (Section 11.6) is

$$\begin{vmatrix} \alpha - E & \beta & 0 & 0 & 0 & \cdots & 0 \\ \beta & \alpha - E & \beta & 0 & 0 & \cdots & 0 \\ 0 & \beta & \alpha - E & \beta & 0 & \cdots & 0 \\ 0 & 0 & \beta & \alpha - E & \beta & \cdots & 0 \\ 0 & 0 & 0 & \beta & \alpha - E & \cdots & 0 \\ \vdots & \vdots & \vdots & \vdots & \vdots & \cdots & \vdots \\ 0 & 0 & 0 & 0 & 0 & \cdots & \alpha - E \end{vmatrix} = 0$$

where β is now the (s,s) resonance integral. The theory of determinants applied to such a symmetrical example as this (technically a ‘tridiagonal determinant’) leads to the following expression for the roots:

$$E_R = \alpha + 2\beta \cos \frac{k\pi}{N+1} \quad k = 1, 2, \dots, N \quad (20.21)$$

When N is infinitely large, the difference between neighbouring energy levels (the energies corresponding to k and $k+1$) is infinitely small, but, as we show in the following *Justification*, the band still has finite width overall:

$$E_N - E_1 \rightarrow 4\beta \quad \text{as } N \rightarrow \infty \quad (20.22)$$

We can think of this band as consisting of N different molecular orbitals, the lowest-energy orbital ($k=1$) being fully bonding, and the highest-energy orbital ($k=N$) being fully antibonding between adjacent atoms (Fig. 20.52). Similar bands form in three-dimensional solids.

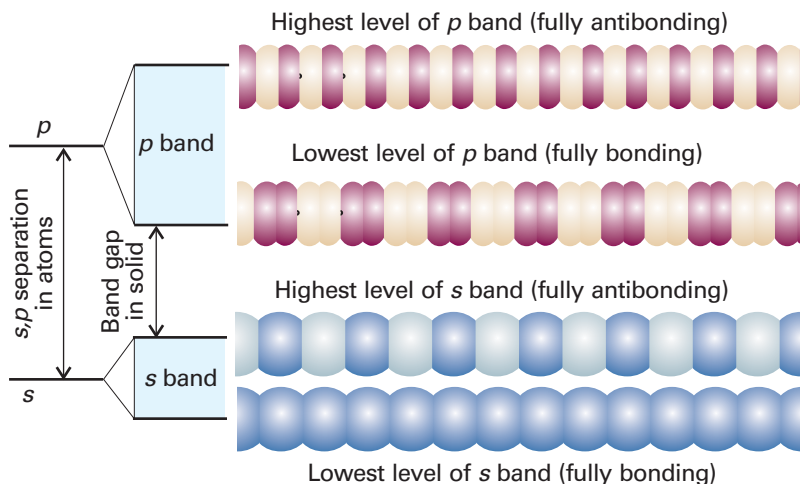


Fig. 20.52 The overlap of *s* orbitals gives rise to an *s* band and the overlap of *p* orbitals gives rise to a *p* band. In this case, the *s* and *p* orbitals of the atoms are so widely spaced that there is a band gap. In many cases the separation is less and the bands overlap.

Justification 20.5 The width of a band

The energy of the level with $k = 1$ is

$$E_1 = \alpha + 2\beta \cos \frac{\pi}{N+1}$$

As N becomes infinite, the cosine term becomes $\cos 0 = 1$. Therefore, in this limit

$$E_1 = \alpha + 2\beta$$

When k has its maximum value of N ,

$$E_N = \alpha + 2\beta \cos \frac{N\pi}{N+1}$$

As N approaches infinity, we can ignore the 1 in the denominator, and the cosine term becomes $\cos \pi = -1$. Therefore, in this limit

$$E_N = \alpha - 2\beta$$

The difference between the upper and lower energies of the band is therefore 4β .

The band formed from overlap of *s* orbitals is called the ***s* band**. If the atoms have *p* orbitals available, the same procedure leads to a ***p* band** (as shown in the upper half of Fig. 20.52). If the atomic *p* orbitals lie higher in energy than the *s* orbitals, then the *p* band lies higher than the *s* band, and there may be a **band gap**, a range of energies to which no orbital corresponds. However, the *s* and *p* bands may also be contiguous or even overlap (as is the case for the $3s$ and $3p$ bands in magnesium).

(b) The occupation of orbitals

Now consider the electronic structure of a solid formed from atoms each able to contribute one electron (for example, the alkali metals). There are N atomic orbitals and therefore N molecular orbitals packed into an apparently continuous band. There are N electrons to accommodate.

At $T = 0$, only the lowest $\frac{1}{2}N$ molecular orbitals are occupied (Fig. 20.53), and the HOMO is called the **Fermi level**. However, unlike in molecules, there are empty orbitals very close in energy to the Fermi level, so it requires hardly any energy to excite the uppermost electrons. Some of the electrons are therefore very mobile and give rise to electrical conductivity.

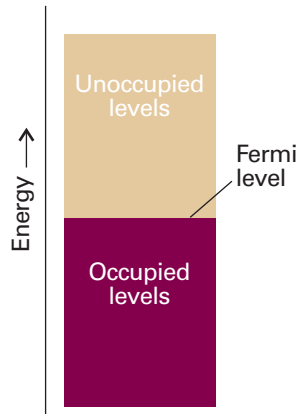


Fig. 20.53 When N electrons occupy a band of N orbitals, it is only half full and the electrons near the Fermi level (the top of the filled levels) are mobile.

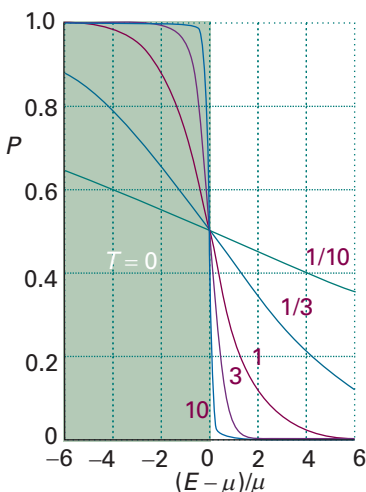


Fig. 20.54 The Fermi-Dirac distribution, which gives the population of the levels at a temperature T . The high-energy tail decays exponentially towards zero. The curves are labelled with the value of μ/kT . The pale green region shows the occupation of levels at $T = 0$.

 **Exploration** Express the population P as a function of the variables $(E - \mu)/\mu$ and μ/kT and then display the set of curves shown in Fig. 20.54 as a single surface.

At temperatures above absolute zero, electrons can be excited by the thermal motion of the atoms. The population, P , of the orbitals is given by the **Fermi-Dirac distribution**, a version of the Boltzmann distribution that takes into account the effect of the Pauli principle:

$$P = \frac{1}{e^{(E-\mu)/kT} + 1} \quad (20.23)$$

The quantity μ is the **chemical potential**, which in this context is the energy of the level for which $P = \frac{1}{2}$ (note that the chemical potential decreases as the temperature increases). The chemical potential in eqn 20.23 has the dimensions of energy, not energy per mole.

The shape of the Fermi-Dirac distribution is shown in Fig. 20.54. For energies well above μ , the 1 in the denominator can be neglected, and then

$$P \approx e^{-(E-\mu)/kT} \quad (20.24)$$

The population now resembles a Boltzmann distribution, decaying exponentially with increasing energy. The higher the temperature, the longer the exponential tail.

The electrical conductivity of a metallic solid decreases with increasing temperature even though more electrons are excited into empty orbitals. This apparent paradox is resolved by noting that the increase in temperature causes more vigorous thermal motion of the atoms, so collisions between the moving electrons and an atom are more likely. That is, the electrons are scattered out of their paths through the solid, and are less efficient at transporting charge.

(c) Insulators and semiconductors

When each atom provides two electrons, the $2N$ electrons fill the N orbitals of the s band. The Fermi level now lies at the top of the band (at $T = 0$), and there is a gap before the next band begins (Fig. 20.55). As the temperature is increased, the tail of the Fermi-Dirac distribution extends across the gap, and electrons leave the lower band, which is called the **valence band**, and populate the empty orbitals of the upper band, which is called the **conduction band**. As a consequence of electron promotion, positively charged ‘holes’ are left in the valence band. The holes and promoted electrons are now mobile, and the solid is an electrical conductor. In fact, it is a semiconductor, because the electrical conductivity depends on the number of electrons that are promoted across the gap, and that number increases as the temperature is raised. If the gap is large, though, very few electrons will be promoted at ordinary temperatures and the conductivity will remain close to zero, resulting in an insulator. Thus, the conventional distinction between an insulator and a semiconductor is related to the size of the band gap and is not an absolute distinction like that between a metal (incomplete bands at $T = 0$) and a semiconductor (full bands at $T = 0$).

Figure 20.55 depicts conduction in an **intrinsic semiconductor**, in which semiconduction is a property of the band structure of the pure material. Examples of intrinsic semiconductors include silicon and germanium. A **compound semiconductor** is an intrinsic semiconductor that is a combination of different elements, such as GaN, CdS, and many d -metal oxides. An **extrinsic semiconductor** is one in which charge carriers are present as a result of the replacement of some atoms (to the extent of about 1 in 10^9) by **dopant** atoms, the atoms of another element. If the dopants can trap electrons, they withdraw electrons from the filled band, leaving holes which allow the remaining electrons to move (Fig. 20.56a). This procedure gives rise to **p-type semconductivity**, the p indicating that the holes are positive relative to the electrons in the band. An example is silicon doped with indium. We can picture the

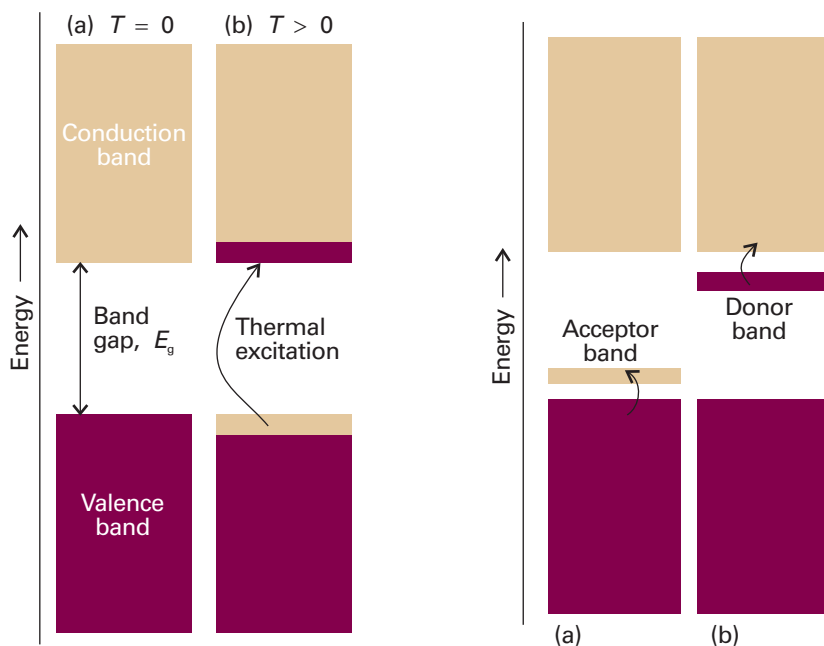


Fig. 20.55 (a) When $2N$ electrons are present, the band is full and the material is an insulator at $T=0$. (b) At temperatures above $T=0$, electrons populate the levels of the upper *conduction band* and the solid is a semiconductor.

Fig. 20.56 (a) A dopant with fewer electrons than its host can form a narrow band that accepts electrons from the valence band. The holes in the band are mobile and the substance is a p-type semiconductor. (b) A dopant with more electrons than its host forms a narrow band that can supply electrons to the conduction band. The electrons it supplies are mobile and the substance is an n-type semiconductor.

semiconduction as arising from the transfer of an electron from a Si atom to a neighbouring In atom. The electrons at the top of the silicon valence band are now mobile, and carry current through the solid. Alternatively, a dopant might carry excess electrons (for example, phosphorus atoms introduced into germanium), and these additional electrons occupy otherwise empty bands, giving **n-type semiconductivity**, where n denotes the negative charge of the carriers (Fig. 20.56b). The preparation of doped but otherwise ultrapure materials was described in *Impact I6.2*.

Now we consider the properties of a **p–n junction**, the interface of a p-type and n-type semiconductor. Consider the application of a ‘reverse bias’ to the junction, in the sense that a negative electrode is attached to the p-type semiconductor and a positive electrode is attached to the n-type semiconductor (Fig. 20.57a). Under these conditions, the positively charged holes in p-type semiconductor are attracted to the negative electrode and the negatively charged electrons in the n-type semiconductor are attracted to the positive electrode. As a consequence, charge does not flow across the junction. Now consider the application of a ‘forward bias’ to the junction, in the sense that the positive electrode is attached to the p-type semiconductor and the negative electrode is attached to the n-type semiconductor (Fig. 20.57b). Now charge flows across the junction, with electrons in the n-type semiconductor moving toward the positive electrode and holes moving in the opposite direction. It follows that a p–n junction affords a great deal of control over the magnitude and direction of current

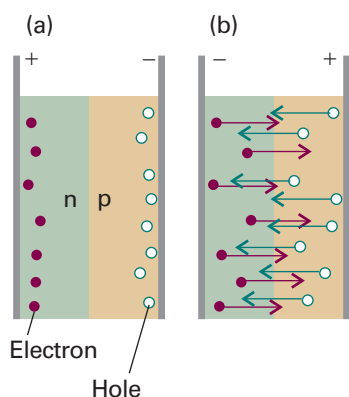


Fig. 20.57 A p–n junction under (a) reverse bias, (b) forward bias.

through a material. This control is essential for the operation of transistors and diodes, which are key components of modern electronic devices.

As electrons and holes move across a p–n junction under forward bias, they recombine and release energy. However, as long as the forward bias continues to be applied, the flow of charge from the electrodes to the semiconductors will replenish them with electrons and holes, so the junction will sustain a current. In some solids, the energy of electron–hole recombination is released as heat and the device becomes warm. This is the case for silicon semiconductors, and is one reason why computers need efficient cooling systems.

IMPACT ON NANOSCIENCE

I20.2 Nanowires

We have already remarked (*Impacts* I19.1, I19.2, and I19.3) that research on nanometre-sized materials is motivated by the possibility that they will form the basis for cheaper and smaller electronic devices. The synthesis of *nanowires*, nanometre-sized atomic assemblies that conduct electricity, is a major step in the fabrication of nanodevices. An important type of nanowire is based on carbon nanotubes, which, like graphite, can conduct electrons through delocalized π molecular orbitals that form from unhybridized $2p$ orbitals on carbon. Recent studies have shown a correlation between structure and conductivity in single-walled nanotubes (SWNTs) that does not occur in graphite. The SWNT in Fig. 20.45 is a semiconductor. If the hexagons are rotated by 90° about their sixfold axis, the resulting SWNT is a metallic conductor.

Carbon nanotubes are promising building blocks not only because they have useful electrical properties but also because they have unusual mechanical properties. For example, an SWNT has a Young's modulus that is approximately five times larger and a tensile strength that is approximately 375 times larger than that of steel.

Silicon nanowires can be made by focusing a pulsed laser beam on to a solid target composed of silicon and iron. The laser ejects Fe and Si atoms from the surface of the target, forming a vapour that can condense into liquid FeSi_n nanoclusters at sufficiently low temperatures. The phase diagram for this complex mixture shows that solid silicon and liquid FeSi_n coexist at temperatures higher than 1473 K. Hence, it is possible to precipitate solid silicon from the mixture if the experimental conditions are controlled to maintain the FeSi_n nanoclusters in a liquid state that is supersaturated with silicon. It is observed that the silicon precipitate consists of nanowires with diameters of about 10 nm and lengths greater than 1 μm .

Nanowires are also fabricated by *molecular beam epitaxy* (MBE), in which gaseous atoms or molecules are sprayed onto a crystalline surface in an ultra-high vacuum chamber. The result is formation of highly ordered structures. Through careful control of the chamber temperature and of the spraying process, it is possible to deposit thin films on to a surface or to create nanometre-sized assemblies with specific shapes. For example, Fig. 20.58 shows an AFM image of germanium nanowires on a silicon surface. The wires are about 2 nm high, 10–32 nm wide, and 10–600 nm long.

Direct manipulation of atoms on a surface also leads to the formation of nanowires. The Coulomb attraction between an atom and the tip of an STM can be exploited to move atoms along a surface, arranging them into patterns, such as wires.

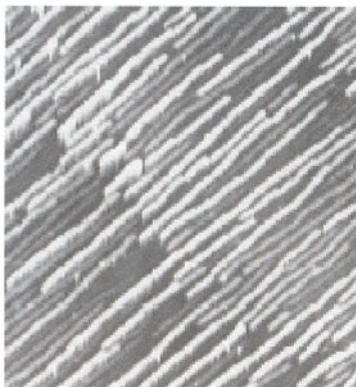


Fig. 20.58 Germanium nanowires fabricated on to a silicon surface by molecular beam epitaxy. (Reproduced with permission from T. Ogino *et al.* *Acc. Chem. Res.* **32**, 447 (1999).)

20.10 Optical properties

In this section, we explore the consequences of interactions between electromagnetic radiation and solids. Our focus will be on the origins of phenomena that inform the design of useful devices, such as lasers and light-emitting diodes.

(a) Light absorption by molecular solids, metallic conductors, and semiconductors

From the discussion in earlier chapters, we are already familiar with the factors that determine the energy and intensity of light absorbed by atoms and molecules in the gas phase and in solution. Now we consider the effects on the electronic absorption spectrum of bringing atoms or molecules together into a solid.

Consider an electronic excitation of a molecule (or an ion) in a crystal. If the excitation corresponds to the removal of an electron from one orbital of a molecule and its elevation to an orbital of higher energy, then the excited state of the molecule can be envisaged as the coexistence of an electron and a hole. This electron–hole pair, the particle-like **exciton**, migrates from molecule to molecule in the crystal (Fig. 20.59). Exciton formation causes spectral lines to shift, split, and change intensity.

The electron and the hole jump together from molecule to molecule as they migrate. A migrating excitation of this kind is called a **Frenkel exciton**. The electron and hole can also be on different molecules, but in each other's vicinity. A migrating excitation of this kind, which is now spread over several molecules (more usually ions), is a **Wannier exciton**.

Frenkel excitons are more common in molecular solids. Their migration implies that there is an interaction between the species that constitute the crystal, for otherwise the excitation on one unit could not move to another. This interaction affects the energy levels of the system. The strength of the interaction governs the rate at which an exciton moves through the crystal: a strong interaction results in fast migration, and a vanishingly small interaction leaves the exciton localized on its original molecule. The specific mechanism of interaction that leads to exciton migration is the interaction between the transition dipole moments of the excitation. Thus, an electric dipole transition in a molecule is accompanied by a shift of charge, and the transient dipole exerts a force on an adjacent molecule. The latter responds by shifting its charge. This process continues and the excitation migrates through the crystal.

The energy shift arising from the interaction between transition dipoles can be understood in terms of their electrostatic interaction. An all-parallel arrangement of the dipoles (Fig. 20.60a) is energetically unfavourable, so the absorption occurs at a higher frequency than in the isolated molecule. Conversely, a head-to-tail alignment of transient dipoles (Fig. 20.60b) is energetically favourable, and the transition occurs at a lower frequency than in the isolated molecules.

Illustration 20.1 Predicting the frequency of exciton absorption in a molecular solid

Recall from Section 18.4 that the potential energy of interaction between two parallel dipoles μ_1 and μ_2 separated by a distance r is $V = \mu_1\mu_2(1 - 3 \cos^2\theta)/4\pi\epsilon_0 r^3$, where the angle θ is defined in (1). We see that $\theta = 0^\circ$ for a head-to-tail alignment and $\theta = 90^\circ$ for a parallel alignment. It follows that $V < 0$ (an attractive interaction) for $0^\circ \leq \theta < 54.74^\circ$, $V = 0$ when $\theta = 54.74^\circ$ (for then $1 - 3 \cos^2\theta = 0$), and $V > 0$ (a repulsive interaction) for $54.74^\circ < \theta \leq 90^\circ$. This result is expected on the basis of qualitative arguments. In a head-to-tail arrangement, the interaction between the region of partial positive charge in one molecule with the region of partial negative charge in the other molecule is attractive. By contrast, in a parallel arrangement, the molecular interaction is repulsive because of the close approach of regions of partial charge with the same sign.

It follows from this discussion that, when $0^\circ \leq \theta < 54.74^\circ$, the frequency of exciton absorption is lower than the corresponding absorption frequency for the isolated molecule (a *red shift* in the spectrum of the solid with respect to that of the isolated

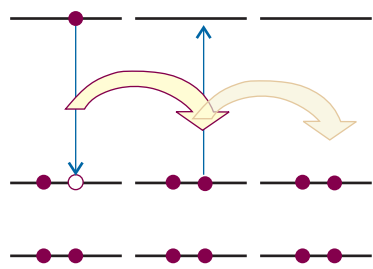


Fig. 20.59 The electron–hole pair shown on the left can migrate through a solid lattice as the excitation hops from molecule to molecule. The mobile excitation is called an exciton.

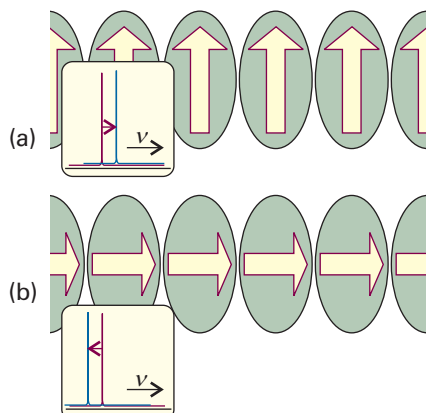
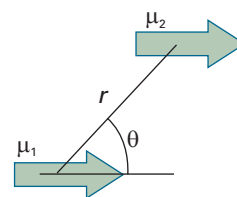


Fig. 20.60 (a) The alignment of transition dipoles (the yellow arrows) is energetically unfavourable, and the exciton absorption is shifted to higher energy (higher frequency). (b) The alignment is energetically favourable for a transition in this orientation, and the exciton band occurs at lower frequency than in the isolated molecules.



molecule). Conversely, when $54.74^\circ < \theta \leq 90^\circ$, the frequency of exciton absorption is higher than the corresponding absorption frequency for the isolated molecule (a *blue shift* in the spectrum of the solid with respect to that of the isolated molecule). In the special case $\theta = 54.74^\circ$ the solid and the isolated molecule have absorption lines at the same frequency.

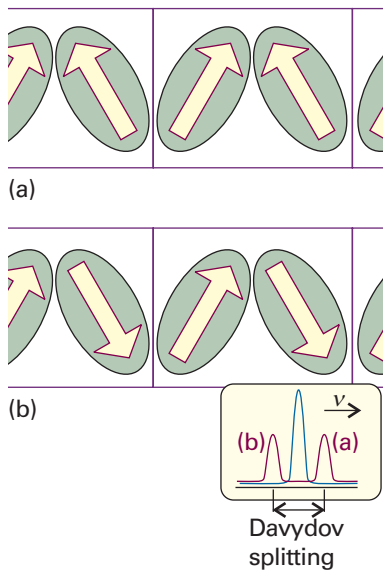


Fig. 20.61 When the transition moments within a unit cell may lie in different relative directions, as depicted in (a) and (b), the energies of the transitions are shifted and give rise to the two bands labelled (a) and (b) in the spectrum. The separation of the bands is the Davydov splitting.

If there are N molecules per unit cell, there are N **exciton bands** in the spectrum (if all of them are allowed). The splitting between the bands is the **Davydov splitting**. To understand the origin of the splitting, consider the case $N = 2$ with the molecules arranged as in Fig. 20.61. Let the transition dipoles be along the length of the molecules. The radiation stimulates the collective excitation of the transition dipoles that are in-phase between neighbouring unit cells. *Within* each unit cell the transition dipoles may be arrayed in the two different ways shown in the illustration. Since the two orientations correspond to different interaction energies, with interaction being repulsive in one and attractive in the other, the two transitions appear in the spectrum at two bands of different frequencies. The Davydov splitting is determined by the energy of interaction between the transition dipoles within the unit cell.

Now we turn our attention to metallic conductors and semiconductors. Again we need to consider the consequences of interactions between particles, in this case atoms, which are now so strong that we need to abandon arguments based primarily on van der Waals interactions in favour of a full molecular orbital treatment, the band model of Section 20.9.

Consider Fig. 20.53, which shows bands in an idealized metallic conductor. The absorption of light can excite electrons from the occupied levels to the unoccupied levels. There is a near continuum of unoccupied energy levels above the Fermi level, so we expect to observe absorption over a wide range of frequencies. In metals, the bands are sufficiently wide that radiation from the radiofrequency to the middle of the ultraviolet region of the electromagnetic spectrum is absorbed (metals are transparent to very high-frequency radiation, such as X-rays and γ -rays). Because this range of absorbed frequencies includes the entire visible spectrum, we expect that all metals should appear black. However, we know that metals are shiny (that is, they reflect light) and some are coloured (that is, they absorb light of only certain wavelengths), so we need to extend our model.

To explain the shiny appearance of a smooth metal surface, we need to realize that the absorbed energy can be re-emitted very efficiently as light, with only a small fraction of the energy being released to the surroundings as heat. Because the atoms near the surface of the material absorb most of the radiation, emission also occurs primarily from the surface. In essence, if the sample is excited with visible light, then visible light will be reflected from the surface, accounting for the lustre of the material.

The perceived colour of a metal depends on the frequency range of reflected light which, in turn, depends on the frequency range of light that can be absorbed and, by extension, on the band structure. Silver reflects light with nearly equal efficiency across the visible spectrum because its band structure has many unoccupied energy levels that can be populated by absorption of, and depopulated by emission of, visible light. On the other hand, copper has its characteristic colour because it has relatively fewer unoccupied energy levels that can be excited with violet, blue, and green light. The material reflects at all wavelengths, but more light is emitted at lower frequencies (corresponding to yellow, orange, and red). Similar arguments account for the colours of other metals, such as the yellow of gold.

Finally, consider semiconductors. We have already seen that promotion of electrons from the valence to the conduction band of a semiconductor can be the result of

thermal excitation, if the band gap E_g is comparable to the energy that can be supplied by heating. In some materials, the band gap is very large and electron promotion can occur only by excitation with electromagnetic radiation. However, we see from Fig. 20.55 that there is a frequency $\nu_{\min} = E_g/h$ below which light absorption cannot occur. Above this frequency threshold, a wide range of frequencies can be absorbed by the material, as in a metal.

Illustration 20.2 Predicting the colour of a semiconductor

The semiconductor cadmium sulfide (CdS) has a band gap energy of 2.4 eV (equivalent to 3.8×10^{-19} J). It follows that the minimum electronic absorption frequency is

$$\nu_{\min} = \frac{3.8 \times 10^{-19} \text{ J}}{6.626 \times 10^{-34} \text{ J}} = 5.8 \times 10^{14} \text{ s}^{-1}$$

This frequency, of 5.8×10^{14} Hz, corresponds to a wavelength of 517 nm (green light; see Table 14.1). Lower frequencies, corresponding to yellow, orange, and red, are not absorbed and consequently CdS appears yellow-orange.

Self-test 20.7 Predict the colours of the following materials, given their band-gap energies (in parentheses): GaAs (1.43 eV), HgS (2.1 eV), and ZnS (3.6 eV). [Black, red, and colourless]

(b) Light emission by solid-state lasers and light-emitting diodes

Here we explore the further consequences of light emission in solids, focusing our attention on ionic crystals and semiconductors used in the design of lasers and light-emitting diodes. In Chapter 14 we discussed the conditions under which a material can become a laser and it would be helpful to review those concepts.

The **neodymium laser** is an example of a four-level laser, in which the laser transition terminates in a state other than the ground state of the laser material (Fig. 20.62). In one form it consists of Nd³⁺ ions at low concentration in yttrium aluminium garnet (YAG, specifically Y₃Al₅O₁₂), and is then known as a **Nd-YAG laser**. The population inversion results from pumping a majority of the Nd³⁺ ions into an excited state by using an intense flash from another source, followed by a radiationless transition to another excited state. The pumping flash need not be monochromatic because the upper level actually consists of several states spanning a band of frequencies. A neodymium laser operates at a number of wavelengths in the infrared, the band at 1064 nm being most common. The transition at 1064 nm is very efficient and the laser is capable of substantial power output, either in continuous or pulsed (by Q-switching or mode-locking as discussed in Section 14.5) modes of operation.

The **titanium sapphire laser** consists of Ti³⁺ ions at low concentration in a crystal of sapphire (Al₂O₃). The electronic absorption spectrum of Ti³⁺ ion in sapphire is very similar to that shown in Fig. 14.13, with a broad absorption band centred at around 500 nm that arises from vibronically allowed *d-d* transitions of the Ti³⁺ ion in an octahedral environment provided by oxygen atoms of the host lattice. As a result, the emission spectrum of Ti³⁺ in sapphire is also broad and laser action occurs over a wide range of wavelengths (Fig. 20.63). Therefore, the titanium sapphire laser is an example of a **vibronic laser**, in which the laser transitions originate from vibronic transitions in the laser medium. The titanium sapphire laser is usually pumped by another laser, such as a Nd-YAG laser or an argon-ion laser (*Further information 14.1*),

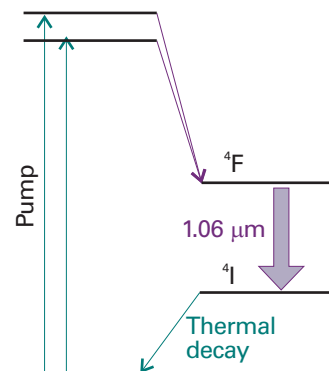


Fig. 20.62 The transitions involved in a neodymium laser. The laser action takes place between the ⁴F and ⁴I excited states.

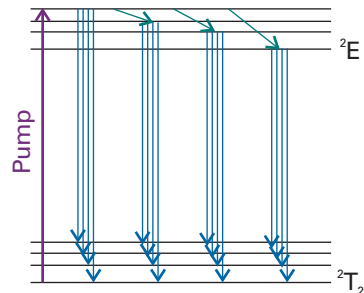


Fig. 20.63 The transitions involved in a titanium sapphire laser. The laser medium consists of sapphire (Al₂O₃) doped with Ti³⁺ ions. Monochromatic light from a pump laser induces a ²E \leftarrow ²T₂ transition in a Ti³⁺ ion that resides in a site with octahedral symmetry. After radiationless vibrational excitation in the ²E state, laser emission occurs from a very large number of closely spaced vibronic states of the medium. As a result, the titanium sapphire laser emits radiation over a broad spectrum that spans from about 700 nm to about 1000 nm.

and can be operated in either a continuous or pulsed fashion. Mode-locked titanium sapphire lasers produce energetic (20 mJ to 1 J) and very short (20–100 fs, 1 fs = 10^{-15} s) pulses. When considered together with broad wavelength tunability (700–1000 nm), these features of the titanium sapphire laser justify its wide use in modern spectroscopy and photochemistry.

The unique electrical properties of p-n junctions between semiconductors can be put to good use in optical devices. In some materials, most notably gallium arsenide, GaAs, energy from electron–hole recombination is released not as heat but is carried away by photons as electrons move across the junction under forward bias. Practical **light-emitting diodes** of this kind are widely used in electronic displays. The wavelength of emitted light depends on the band gap of the semiconductor. Gallium arsenide itself emits infrared light, but the band gap is widened by incorporating phosphorus, and a material of composition approximately $\text{GaAs}_{0.6}\text{P}_{0.4}$ emits light in the red region of the spectrum.

A light-emitting diode is not a laser, because no resonance cavity and stimulated emission are involved. In **diode lasers**, light emission due to electron–hole recombination is employed as the basis of laser action. The population inversion can be sustained by sweeping away the electrons that fall into the holes of the p-type semiconductor, and a resonant cavity can be formed by using the high refractive index of the semiconducting material and cleaving single crystals so that the light is trapped by the abrupt variation of refractive index. One widely used material is $\text{Ga}_{1-x}\text{Al}_x\text{As}$, which produces infrared laser radiation and is widely used in compact-disc (CD) players.

High-power diode lasers are also used to pump other lasers. One example is the pumping of Nd:YAG lasers by $\text{Ga}_{0.91}\text{Al}_{0.09}\text{As}/\text{Ga}_{0.7}\text{Al}_{0.3}\text{As}$ diode lasers. The Nd:YAG laser is often used to pump yet another laser, such as a Ti:sapphire laser. As a result, it is now possible to construct a laser system for steady-state or time-resolved spectroscopy entirely out of solid-state components.

(c) Nonlinear optical phenomena

Nonlinear optical phenomena arise from changes in the optical properties of a material in the presence of an intense electric field from electromagnetic radiation. Here we explore two phenomena that not only can be studied conveniently with intense laser beams but are commonly used in the laboratory to modify the output of lasers for specific experiments, such as those described in Section 14.6.

In **frequency doubling**, or **second harmonic generation**, an intense laser beam is converted to radiation with twice (and in general a multiple) of its initial frequency as it passes through a suitable material. It follows that frequency doubling and tripling of a Nd-YAG laser, which emits radiation at 1064 nm, produce green light at 532 nm and ultraviolet radiation at 355 nm, respectively.

We can account for frequency doubling by examining how a substance responds nonlinearly to incident radiation of frequency $\omega = 2\pi\nu$. Radiation of a particular frequency arises from oscillations of an electric dipole at that frequency and the incident electric field E induces an electric dipole of magnitude μ , in the substance. At low light intensity, most materials respond linearly, in the sense that $\mu = \alpha E$, where α is the polarizability (see Section 18.2). To allow for nonlinear response by some materials at high light intensity, we can write

$$\mu = \alpha E + \frac{1}{2} \beta E^2 + \dots \quad (20.25)$$

where the coefficient β is the **hyperpolarizability** of the material. The nonlinear term βE^2 can be expanded as follows if we suppose that the incident electric field is $E_0 \cos \omega t$:

$$\beta E^2 = \beta E_0^2 \cos^2 \omega t = \frac{1}{2} \beta E_0^2 (1 + \cos 2\omega t) \quad (20.26)$$

Hence, the nonlinear term contributes an induced electric dipole that oscillates at the frequency 2ω and that can act as a source of radiation of that frequency. Common materials that can be used for frequency doubling in laser systems include crystals of potassium dihydrogenphosphate (KH_2PO_4), lithium niobate (LiNbO_3), and β -barium borate ($\beta\text{-BaB}_2\text{O}_4$).

Another important nonlinear optical phenomenon is the **optical Kerr effect**, which arises from a change in refractive index of a well chosen medium, the **Kerr medium**, when it is exposed to intense laser pulses. Because a beam of light changes direction when it passes from a region of one refractive index to a region with a different refractive index, changes in refractive index result in the self-focusing of an intense laser pulse as it travels through the Kerr medium (Fig. 20.64).

The optical Kerr effect is used as a mechanism of mode-locking lasers (Section 14.5). A Kerr medium is included in the cavity and next to it is a small aperture. The procedure makes use of the fact that the **gain**, the growth in intensity, of a frequency component of the radiation in the cavity is very sensitive to amplification and, once a particular frequency begins to grow, it can quickly dominate. When the power inside the cavity is low, a portion of the photons will be blocked by the aperture, creating a significant loss. A spontaneous fluctuation in intensity—a bunching of photons—may begin to turn on the optical Kerr effect and the changes in the refractive index of the Kerr medium will result in a **Kerr lens**, which is the self-focusing of the laser beam. The bunch of photons can pass through and travel to the far end of the cavity, amplifying as it goes. The Kerr lens immediately disappears (if the medium is well chosen), but is re-created when the intense pulse returns from the mirror at the far end. In this way, that particular bunch of photons may grow to considerable intensity because it alone is stimulating emission in the cavity. Sapphire is an example of a Kerr medium that facilitates the mode locking of titanium sapphire lasers, resulting in very short laser pulses of duration in the femtosecond range.

In addition to being useful laboratory tools, nonlinear optical materials are also finding many applications in the telecommunications industry, which is becoming ever more reliant on optical signals transmitted through optical fibres to carry voice and data. Judicious use of nonlinear phenomena leads to more ways in which the properties of optical signals, and hence the information they carry, can be manipulated.

20.11 Magnetic properties

The magnetic properties of metallic solids and semiconductors depend strongly on the band structures of the material (see *Further reading*). Here we confine our attention largely to magnetic properties that stem from collections of individual molecules or ions such as d -metal complexes. Much of the discussion applies to liquid and gas phase samples as well as to solids.

(a) Magnetic susceptibility

The magnetic and electric properties of molecules and solids are analogous. For instance, some molecules possess permanent magnetic dipole moments, and an applied magnetic field can induce a magnetic moment, with the result that the entire solid sample becomes magnetized. The analogue of the electric polarization, P , is the **magnetization**, \mathcal{M} , the average molecular magnetic dipole moment multiplied by the number density of molecules in the sample. The magnetization induced by a field of strength H is proportional to H , and we write

$$\mathcal{M} = \chi H \quad [20.27]$$

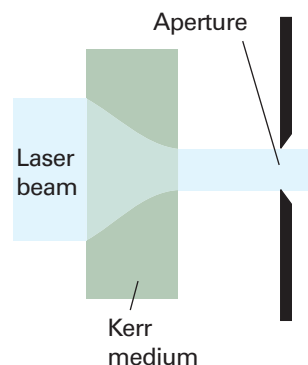


Fig. 20.64 An illustration of the Kerr effect. An intense laser beam is focused inside a Kerr medium and passes through a small aperture in the laser cavity. This effect may be used to mode-lock a laser, as explained in the text.

where χ is the dimensionless **volume magnetic susceptibility**. A closely related quantity is the **molar magnetic susceptibility**, χ_m :

$$\chi_m = \chi V_m \quad [20.28]$$

where V_m is the molar volume of the substance (we shall soon see why it is sensible to introduce this quantity). The **magnetic flux density**, B , is related to the applied field strength and the magnetization by

$$B = \mu_0(H + M) = \mu_0(1 + \chi)H \quad [20.29]$$

where μ_0 is the vacuum permeability, $\mu_0 = 4\pi \times 10^{-7} \text{ J C}^{-2} \text{ m}^{-1} \text{ s}^2$. The magnetic flux density can be thought of as the density of magnetic lines of force permeating the medium. This density is increased if M adds to H (when $\chi > 0$), but the density is decreased if M opposes H (when $\chi < 0$). Materials for which χ is positive are called **paramagnetic**. Those for which χ is negative are called **diamagnetic**.

Just as polar molecules in fluid phases contribute a term proportional to $\mu^2/3kT$ to the electric polarization of a medium (eqn 18.15), so molecules with a permanent magnetic dipole moment of magnitude m contribute to the magnetization an amount proportional to $m^2/3kT$. However, unlike for polar molecules, this contribution to the magnetization is obtained even for paramagnetic species trapped in solids, because the direction of the spin of the electrons is typically not coupled to the orientation of the molecular framework and so contributes even when the nuclei are stationary. An applied field can also induce a magnetic moment by stirring up currents in the electron distribution like those responsible for the chemical shift in NMR (Section 15.5). The constant of proportionality between the induced moment and the applied field is called the **magnetizability**, ξ (xi), and the magnetic analogue of eqn 18.15 is

$$\chi = \mathcal{N}\mu_0 \left(\xi + \frac{m^2}{3kT} \right) \quad (20.30)$$

We can now see why it is convenient to introduce χ_m , because the product of the number density \mathcal{N} and the molar volume is Avogadro's constant, N_A :

$$\mathcal{N}V_m = \frac{NV_m}{V} = \frac{nN_A V_m}{nV_m} = N_A \quad (20.31)$$

Hence

$$\chi_m = N_A \mu_0 \left(\xi + \frac{m^2}{3kT} \right) \quad (20.32)$$

and the density dependence of the susceptibility (which occurs in eqn 20.30 via $\mathcal{N} = N_A \rho/M$) has been eliminated. The expression for χ_m is in agreement with the empirical **Curie law**:

$$\chi_m = A + \frac{C}{T} \quad (20.33)$$

with $A = N_A \mu_0 \xi$ and $C = N_A \mu_0 m^2/3k$. As indicated above, and in contrast to electric moments, this expression applies to solids as well as fluid phases.

The magnetic susceptibility is traditionally measured with a **Gouy balance**. This instrument consists of a sensitive balance from which the sample hangs in the form of a narrow cylinder and lies between the poles of a magnet. If the sample is paramagnetic, it is drawn into the field, and its apparent weight is greater than when the field is off. A diamagnetic sample tends to be expelled from the field and appears to weigh less when the field is turned on. The balance is normally calibrated against a sample of

Synoptic table 20.6* Magnetic susceptibilities at 298 K

	$\chi/10^{-6}$	$\chi_m/(10^{-5} \text{ cm}^3 \text{ mol}^{-1})$
$\text{H}_2\text{O(l)}$	-9.06	-160
NaCl(s)	-13.9	-38
Cu(s)	-9.6	-6.8
$\text{CuSO}_4 \cdot 5\text{H}_2\text{O(s)}$	+176	+1930

* More values are given in the *Data section*.

known susceptibility. The modern version of the determination makes use of a **superconducting quantum interference device** (SQUID, Fig. 20.65). A SQUID takes advantage of the quantization of magnetic flux and the property of current loops in superconductors that, as part of the circuit, include a weakly conducting link through which electrons must tunnel. The current that flows in the loop in a magnetic field depends on the value of the magnetic flux, and a SQUID can be exploited as a very sensitive magnetometer.

Table 20.6 lists some experimental values. A typical paramagnetic volume susceptibility is about 10^{-3} , and a typical diamagnetic volume susceptibility is about $(-)10^{-5}$. The permanent magnetic moment can be extracted from susceptibility measurements by plotting χ against $1/T$.

(b) The permanent magnetic moment

The permanent magnetic moment of a molecule arises from any unpaired electron spins in the molecule. We saw in Section 10.8 that the magnitude of the magnetic moment of an electron is proportional to the magnitude of the spin angular momentum, $\{s(s+1)\}^{1/2}\hbar$.

$$\mu = g_e \{s(s+1)\}^{1/2} \mu_B \quad \mu_B = \frac{e\hbar}{2m_e} \quad (20.34)$$

where $g_e = 2.0023$ (see Section 15.1). If there are several electron spins in each molecule, they combine to a total spin S , and then $s(s+1)$ should be replaced by $S(S+1)$. It follows that the spin contribution to the molar magnetic susceptibility is

$$\chi_m = \frac{N_A g_e^2 \mu_0 \mu_B^2 S(S+1)}{3kT} \quad (20.35)$$

This expression shows that the susceptibility is positive, so the spin magnetic moments contribute to the paramagnetic susceptibilities of materials. The contribution decreases with increasing temperature because the thermal motion randomizes the spin orientations. In practice, a contribution to the paramagnetism also arises from the orbital angular momenta of electrons: we have discussed the spin-only contribution.

Illustration 20.3 Calculating a magnetic susceptibility

Consider a complex salt with three unpaired electrons per complex cation at 298 K, of mass density 3.24 g cm^{-3} , and molar mass 200 g mol^{-1} . First note that

$$\frac{N_A g_e^2 \mu_0 \mu_B^2}{3k} = 6.3001 \times 10^{-6} \text{ m}^3 \text{ K}^{-1} \text{ mol}^{-1}$$

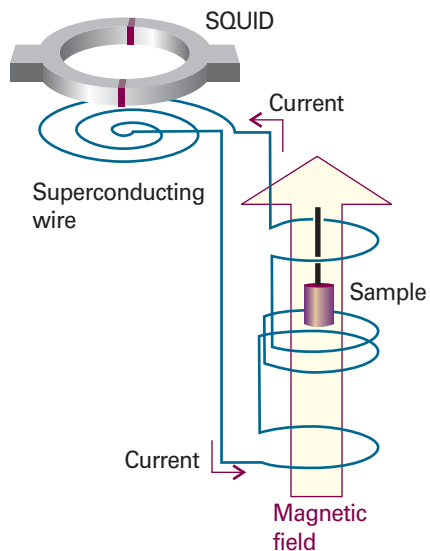


Fig. 20.65 The arrangement used to measure magnetic susceptibility with a SQUID. The sample is moved upwards in small increments and the potential difference across the SQUID is measured.

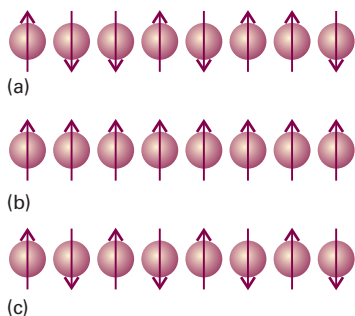


Fig. 20.66 (a) In a paramagnetic material, the electron spins are aligned at random in the absence of an applied magnetic field. (b) In a ferromagnetic material, the electron spins are locked into a parallel alignment over large domains. (c) In an antiferromagnetic material, the electron spins are locked into an antiparallel arrangement. The latter two arrangements survive even in the absence of an applied field.

Consequently,

$$\chi_m = 6.3001 \times 10^{-6} \times \frac{S(S+1)}{T/K} \text{ m}^3 \text{ mol}^{-1}$$

Substitution of the data with $S = \frac{3}{2}$ gives $\chi_m = 7.9 \times 10^{-8} \text{ m}^3 \text{ mol}^{-1}$. Note that the density is not needed at this stage. To obtain the volume magnetic susceptibility, the molar susceptibility is divided by the molar volume $V_m = M/\rho$, where ρ is the mass density. In this illustration, $V_m = 61.7 \text{ cm}^3 \text{ mol}^{-1}$, so $\chi = 1.3 \times 10^{-3}$.

At low temperatures, some paramagnetic solids make a phase transition to a state in which large domains of spins align with parallel orientations. This cooperative alignment gives rise to a very strong magnetization and is called **ferromagnetism** (Fig. 20.66). In other cases, the cooperative effect leads to alternating spin orientations: the spins are locked into a low-magnetization arrangement to give an **antiferromagnetic phase**. The ferromagnetic phase has a nonzero magnetization in the absence of an applied field, but the antiferromagnetic phase has a zero magnetization because the spin magnetic moments cancel. The ferromagnetic transition occurs at the **Curie temperature**, and the antiferromagnetic transition occurs at the **Néel temperature**.

(c) Induced magnetic moments

An applied magnetic field induces the circulation of electronic currents. These currents give rise to a magnetic field that usually opposes the applied field, so the substance is diamagnetic. In a few cases the induced field augments the applied field, and the substance is then paramagnetic.

The great majority of molecules with no unpaired electron spins are diamagnetic. In these cases, the induced electron currents occur within the orbitals of the molecule that are occupied in its ground state. In the few cases in which molecules are paramagnetic despite having no unpaired electrons, the induced electron currents flow in the opposite direction because they can make use of unoccupied orbitals that lie close to the HOMO in energy. This orbital paramagnetism can be distinguished from spin paramagnetism by the fact that it is temperature independent: this is why it is called **temperature-independent paramagnetism** (TIP).

We can summarize these remarks as follows. All molecules have a diamagnetic component to their susceptibility, but it is dominated by spin paramagnetism if the molecules have unpaired electrons. In a few cases (where there are low-lying excited states) TIP is strong enough to make the molecules paramagnetic even though their electrons are paired.

20.12 Superconductors

The resistance to flow of electrical current of a normal metallic conductor decreases smoothly with temperature but never vanishes. However, certain solids known as **superconductors** conduct electricity without resistance below a critical temperature, T_c . Following the discovery in 1911 that mercury is a superconductor below 4.2 K, the boiling point of liquid helium, physicists and chemists made slow but steady progress in the discovery of superconductors with higher values of T_c . Metals, such as tungsten, mercury, and lead, tend to have T_c values below about 10 K. Intermetallic compounds, such as Nb_3X ($\text{X} = \text{Sn}, \text{Al}$, or Ge), and alloys, such as Nb/Ti and Nb/Zr , have intermediate T_c values ranging between 10 K and 23 K. In 1986, **high-temperature superconductors** (HTSC) were discovered. Several **ceramics**, inorganic powders that have

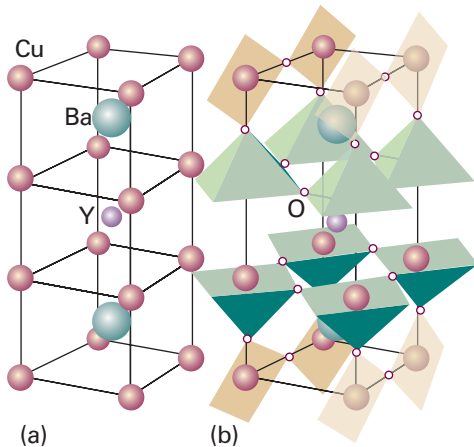


Fig. 20.67 Structure of the $\text{YBa}_2\text{Cu}_3\text{O}_7$ superconductor. (a) Metal atom positions. (b) The polyhedra show the positions of oxygen atoms and indicate that the metal ions are in square-planar and square-pyramidal coordination environments.

been fused and hardened by heating to a high temperature, containing oxocuprate motifs, Cu_mO_n , are now known with T_c values well above 77 K, the boiling point of the inexpensive refrigerant liquid nitrogen. For example, $\text{HgBa}_2\text{Ca}_2\text{Cu}_2\text{O}_8$ has $T_c = 153$ K.

Superconductors have unique magnetic properties as well. Some superconductors, classed as **Type I**, show abrupt loss of superconductivity when an applied magnetic field exceeds a critical value H_c characteristic of the material. It is observed that the value of H_c depends on temperature and T_c as

$$H_c(T) = H_c(0) \left(1 - \frac{T^2}{T_c^2} \right) \quad (20.36)$$

where $H_c(0)$ is the value of H_c as $T \rightarrow 0$. Type I superconductors are also completely diamagnetic below H_c , meaning that no magnetic field lines penetrate into the material. This complete exclusion of a magnetic field in a material is known as the **Meissner effect**, which can be visualized by the levitation of a superconductor above a magnet. **Type II** superconductors, which include the HTSCs, show a gradual loss of superconductivity and diamagnetism with increasing magnetic field.

There is a degree of periodicity in the elements that exhibit superconductivity. The metals iron, cobalt, nickel, copper, silver, and gold do not display superconductivity, nor do the alkali metals. It is observed that, for simple metals, ferromagnetism and superconductivity never coexist, but in some of the oxocuprate superconductors ferromagnetism and superconductivity can coexist. One of the most widely studied oxocuprate superconductors $\text{YBa}_2\text{Cu}_3\text{O}_7$ (informally known as ‘123’ on account of the proportions of the metal atoms in the compound) has the structure shown in Fig. 20.67. The square-pyramidal CuO_5 units arranged as two-dimensional layers and the square planar CuO_4 units arranged in sheets are common structural features of oxocuprate HTSCs.

The mechanism of superconductivity is well-understood for low-temperature materials but there is as yet no settled explanation of high-temperature superconductivity. The central concept of low-temperature superconductivity is the existence of a **Cooper pair**, a pair of electrons that exists on account of the indirect electron–electron interactions fostered by the nuclei of the atoms in the lattice. Thus, if one electron is in a particular region of a solid, the nuclei there move toward it to give a distorted local structure (Fig. 20.68). Because that local distortion is rich in positive charge, it is favourable for a second electron to join the first. Hence, there is a virtual attraction between the two electrons, and they move together as a pair. The local distortion can be easily disrupted by thermal motion of the ions in the solid, so the virtual attraction

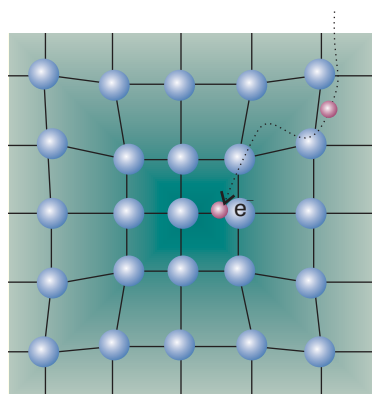


Fig. 20.68 The formation of a Cooper pair. One electron distorts the crystal lattice and the second electron has a lower energy if it goes to that region. These electron–lattice interactions effectively bind the two electrons into a pair.

occurs only at very low temperatures. A Cooper pair undergoes less scattering than an individual electron as it travels through the solid because the distortion caused by one electron can attract back the other electron should it be scattered out of its path in a collision. Because the Cooper pair is stable against scattering, it can carry charge freely through the solid, and hence give rise to superconductivity.

The Cooper pairs responsible for low-temperature superconductivity are likely to be important in HTSCs, but the mechanism for pairing is hotly debated. There is evidence implicating the arrangement of CuO₅ layers and CuO₄ sheets in the mechanism of high-temperature superconductivity. It is believed that movement of electrons along the linked CuO₄ units accounts for superconductivity, whereas the linked CuO₅ units act as ‘charge reservoirs’ that maintain an appropriate number of electrons in the superconducting layers.

Superconductors can sustain large currents and, consequently, are excellent materials for the high-field magnets used in modern NMR spectroscopy (Chapter 15). However, the potential uses of superconducting materials are not limited to the field to chemical instrumentation. For example, HTSCs with T_c values near ambient temperature would be very efficient components of an electrical power transmission system, in which energy loss due to electrical resistance would be minimized. The appropriate technology is not yet available, but research in this area of materials science is active.

Checklist of key ideas

- 1. Solids are classified as metallic, ionic, covalent, and molecular.
- 2. A space lattice is the pattern formed by points representing the locations of structural motifs (atoms, molecules, or groups of atoms, molecules, or ions). The Bravais lattices are the 14 distinct space lattices in three dimensions (Fig. 20.8).
- 3. A unit cell is an imaginary parallelepiped that contains one unit of a translationally repeating pattern. Unit cells are classified into seven crystal systems according to their rotational symmetries.
- 4. Crystal planes are specified by a set of Miller indices (hkl) and the separation of neighbouring planes in a rectangular lattice is given by $1/d_{hkl}^2 = h^2/a^2 + k^2/b^2 + l^2/c^2$.
- 5. Bragg's law relating the glancing angle θ to the separation of lattice planes is $\lambda = 2d \sin \theta$, where λ is the wavelength of the radiation.
- 6. The scattering factor is a measure of the ability of an atom to diffract radiation (eqn 20.6).
- 7. The structure factor is the overall amplitude of a wave diffracted by the { hkl } planes (eqn 20.7). Fourier synthesis is the construction of the electron density distribution from structure factors (eqn 20.8).
- 8. A Patterson synthesis is a map of interatomic vectors obtained by Fourier analysis of diffraction intensities (eqn 20.9).
- 9. Structure refinement is the adjustment of structural parameters to give the best fit between the observed intensities and those calculated from the model of the structure deduced from the diffraction pattern.
- 10. Many elemental metals have close-packed structures with coordination number 12; close-packed structures may be either cubic (ccp) or hexagonal (hcp).
- 11. Representative ionic structures include the caesium-chloride, rock-salt, and zinc-blende structures.
- 12. The radius-ratio rule may be used cautiously to predict which of these three structures is likely (eqn 20.12).
- 13. The lattice enthalpy is the change in enthalpy (per mole of formula units) accompanying the complete separation of the components of the solid. The electrostatic contribution to the lattice enthalpy is expressed by the Born–Mayer equation (eqn 20.15).
- 14. A covalent network solid is a solid in which covalent bonds in a definite spatial orientation link the atoms in a network extending through the crystal. A molecular solid is a solid consisting of discrete molecules held together by van der Waals interactions.
- 15. The mechanical properties of a solid are discussed in terms of the relationship between stress, the applied force divided by the area to which it is applied, and strain, the distortion of a sample resulting from an applied stress.
- 16. The response of a solid to an applied stress is summarized by the Young's modulus (eqn 20.16a), the bulk modulus (eqn 20.16b), the shear modulus (eqn 20.16c), and Poisson's ratio (eqn 20.17).
- 17. Electronic conductors are classified as metallic conductors or semiconductors according to the temperature dependence of their conductivities. An insulator is a semiconductor with a very low electrical conductivity.

18. According to the band theory, electrons occupy molecular orbitals formed from the overlap of atomic orbitals: full bands are called valence bands and empty bands are called conduction bands. The occupation of the orbitals in a solid is given by the Fermi–Dirac distribution (eqn 20.23).
19. Semiconductors are classified as p-type or n-type according to whether conduction is due to holes in the valence band or electrons in the conduction band.
20. The spectroscopic properties of molecular solids can be understood in terms of the formation and migration of excitons, electron–hole pairs, from molecule to molecule.
21. The spectroscopic properties of metallic conductors and semiconductors can be understood in terms of the light-induced promotion of electrons from valence bands to conduction bands.
22. Examples of solid state lasers include the neodymium laser, the titanium sapphire laser, and diode lasers.
23. Nonlinear optical phenomena arise from changes in the optical properties of a material in the presence of an intense field from electromagnetic radiation. Examples include second harmonic generation, and the optical Kerr effect.
24. A bulk sample exposed to a magnetic field of strength H acquires a magnetization, $\mathcal{M} = \chi H$, where χ is the dimensionless volume magnetic susceptibility. When $\chi < 0$, the material is diamagnetic and moves out of a magnetic field. When $\chi > 0$, the material is paramagnetic and moves into a magnetic field.
25. The temperature dependence of χ_m is given by the Curie law $\chi_m = A + C/T$, where $A = N_A \mu_0 \xi$, $C = N_A \mu_0 m^2 / 3k$, and ξ is the magnetizability, a measure of the extent to which a magnetic dipole moment may be induced in a molecule.
26. Ferromagnetism is the cooperative alignment of electron spins in a material and gives rise to strong magnetization. Antiferromagnetism results from alternating spin orientations in a material and leads to weak magnetization.
27. Temperature-independent paramagnetism arises from induced electron currents within the orbitals of a molecule that are occupied in its ground state.
28. Superconductors conduct electricity without resistance below a critical temperature T_c . Type I superconductors show abrupt loss of superconductivity when an applied magnetic field exceeds a critical value H_c characteristic of the material. They are also completely diamagnetic below H_c . Type II superconductors show a gradual loss of superconductivity and diamagnetism with increasing magnetic field.

Further reading

Articles and texts

- C.D. Graham, Jr., Magnetic materials. In *Encyclopedia of applied physics*, G.L. Trigg (ed.), 9, 1 VCH, New York (1994).
- W.B. Pearson and C. Chieh, Crystallography. In *Encyclopedia of applied physics*, G.L. Trigg (ed.), 4, 385 VCH, New York (1992).
- W.D. Callister, Jr., *Materials science and engineering: an introduction*. Wiley, New York (2000).
- P.A. Cox, *The electronic structure and chemistry of solids*. Oxford University Press (1987).

- O. Svelto, *Principles of lasers*. Plenum, New York (1998).
- M.A. White, *Properties of materials*. Oxford University Press (2000).

Sources of data and information

- D.R. Lide (ed.), *CRC Handbook of Chemistry and Physics*, Sections 3, 12, 13, and 15, CRC Press, Boca Raton (2000).
- D. Sangeeta and J.R. LaGraff, *Inorganic materials chemistry desk reference*, CRC Press, Boca Raton (2004).

Discussion questions

- 20.1** Explain how planes of lattice points are labelled.
- 20.2** Describe the procedure for identifying the type and size of a cubic unit cell.
- 20.3** What is meant by a systematic absence? How do they arise?
- 20.4** Describe the phase problem and explain how it may be overcome.
- 20.5** Describe the structures of elemental metallic solids in terms of the packing of hard spheres. To what extent is the hard-sphere model inaccurate?
- 20.6** Describe the caesium-chloride and rock-salt structures in terms of the occupation of holes in expanded close-packed lattices.
- 20.7** Explain how X-ray diffraction can be used to determine the absolute configuration of molecules.
- 20.8** Explain how metallic conductors and semiconductors are identified and explain their electrical and optical properties in terms of band theory.
- 20.9** Describe the characteristics of the Fermi–Dirac distribution. Why is it appropriate to call the parameter μ a chemical potential?
- 20.10** To what extent are the electric and magnetic properties of molecules analogous? How do they differ?

Exercises

20.1a Equivalent lattice points within the unit cell of a Bravais lattice have identical surroundings. What points within a face-centred cubic unit cell are equivalent to the point $(\frac{1}{2}, 0, 0)$?

20.1b Equivalent lattice points within the unit cell of a Bravais lattice have identical surroundings. What points within a body-centred cubic unit cell are equivalent to the point $(\frac{1}{2}, 0, \frac{1}{2})$?

20.2a Find the Miller indices of the planes that intersect the crystallographic axes at the distances $(2a, 3b, 2c)$ and $(2a, 2b, \infty c)$.

20.2b Find the Miller indices of the planes that intersect the crystallographic axes at the distances $(1a, 3b, -c)$ and $(2a, 3b, 4c)$.

20.3a Calculate the separations of the planes $\{111\}$, $\{211\}$, and $\{100\}$ in a crystal in which the cubic unit cell has side 432 pm.

20.3b Calculate the separations of the planes $\{121\}$, $\{221\}$, and $\{244\}$ in a crystal in which the cubic unit cell has side 523 pm.

20.4a The glancing angle of a Bragg reflection from a set of crystal planes separated by 99.3 pm is 20.85° . Calculate the wavelength of the X-rays.

20.4b The glancing angle of a Bragg reflection from a set of crystal planes separated by 128.2 pm is 19.76° . Calculate the wavelength of the X-rays.

20.5a What are the values of 2θ of the first three diffraction lines of bcc iron (atomic radius 126 pm) when the X-ray wavelength is 58 pm?

20.5b What are the values of 2θ of the first three diffraction lines of fcc gold (atomic radius 144 pm) when the X-ray wavelength is 154 pm?

20.6a Copper K_α radiation consists of two components of wavelengths 154.433 pm and 154.051 pm. Calculate the separation of the diffraction lines arising from the two components in a powder diffraction pattern recorded in a circular camera of radius 5.74 cm (with the sample at the centre) from planes of separation 77.8 pm.

20.6b A synchrotron source produces X-radiation at a range of wavelengths. Consider two components of wavelengths 95.401 and 96.035 pm. Calculate the separation of the diffraction lines arising from the two components in a powder diffraction pattern recorded in a circular camera of radius 5.74 cm (with the sample at the centre) from planes of separation 82.3 pm.

20.7a The compound Rb_3TlF_6 has a tetragonal unit cell with dimensions $a = 651$ pm and $c = 934$ pm. Calculate the volume of the unit cell.

20.7b Calculate the volume of the hexagonal unit cell of sodium nitrate, for which the dimensions are $a = 1692.9$ pm and $c = 506.96$ pm.

20.8a The orthorhombic unit cell of $NiSO_4$ has the dimensions $a = 634$ pm, $b = 784$ pm, and $c = 516$ pm, and the density of the solid is estimated as 3.9 g cm^{-3} . Determine the number of formula units per unit cell and calculate a more precise value of the density.

20.8b An orthorhombic unit cell of a compound of molar mass $135.01 \text{ g mol}^{-1}$ has the dimensions $a = 589$ pm, $b = 822$ pm, and $c = 798$ pm. The density of the solid is estimated as 2.9 g cm^{-3} . Determine the number of formula units per unit cell and calculate a more precise value of the density.

20.9a The unit cells of $SbCl_3$ are orthorhombic with dimensions $a = 812$ pm, $b = 947$ pm, and $c = 637$ pm. Calculate the spacing, d , of the $\{411\}$ planes.

20.9b An orthorhombic unit cell has dimensions $a = 679$ pm, $b = 879$ pm, and $c = 860$ pm. Calculate the spacing, d , of the $\{322\}$ planes.

20.10a A substance known to have a cubic unit cell gives reflections with CuK_α radiation (wavelength 154 pm) at glancing angles 19.4° , 22.5° , 32.6° , and

39.4° . The reflection at 32.6° is known to be due to the $\{220\}$ planes. Index the other reflections.

20.10b A substance known to have a cubic unit cell gives reflections with radiation of wavelength 137 pm at the glancing angles 10.7° , 13.6° , 17.7° , and 21.9° . The reflection at 17.7° is known to be due to the $\{111\}$ planes. Index the other reflections.

20.11a Potassium nitrate crystals have orthorhombic unit cells of dimensions $a = 542$ pm, $b = 917$ pm, and $c = 645$ pm. Calculate the glancing angles for the $\{100\}$, $\{010\}$, and $\{111\}$ reflections using CuK_α radiation (154 pm).

20.11b Calcium carbonate crystals in the form of aragonite have orthorhombic unit cells of dimensions $a = 574.1$ pm, $b = 796.8$ pm, and $c = 495.9$ pm. Calculate the glancing angles for the $\{100\}$, $\{010\}$, and $\{111\}$ reflections using radiation of wavelength 83.42 pm (from aluminium).

20.12a Copper(I) chloride forms cubic crystals with four formula units per unit cell. The only reflections present in a powder photograph are those with either all even indices or all odd indices. What is the (Bravais) lattice type of the unit cell?

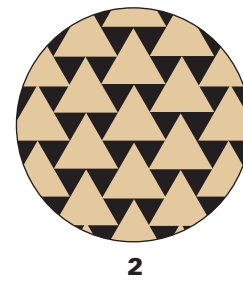
20.12b A powder diffraction photograph from tungsten shows lines that index as $\{110\}$, $\{200\}$, $\{211\}$, $\{220\}$, $\{310\}$, $\{222\}$, $\{321\}$, $\{400\}$, ... Identify the (Bravais) lattice type of the unit cell.

20.13a The coordinates, in units of a , of the atoms in a body-centred cubic lattice are $(0,0,0)$, $(0,1,0)$, $(0,0,1)$, $(0,1,1)$, $(1,0,0)$, $(1,1,0)$, $(1,0,1)$, and $(1,1,1)$. Calculate the structure factors F_{hkl} when all the atoms are identical.

20.13b The coordinates, in units of a , of the atoms in a body-centred cubic lattice are $(0,0,0)$, $(0,1,0)$, $(0,0,1)$, $(0,1,1)$, $(1,0,0)$, $(1,1,0)$, $(1,0,1)$, and $(1,\frac{1}{2},\frac{1}{2},\frac{1}{2})$. Calculate the structure factors F_{hkl} when all the atoms are identical.

20.14a Calculate the packing fraction for close-packed cylinders.

20.14b Calculate the packing fraction for equilateral triangular rods stacked as shown in 2.



20.15a Verify that the radius ratios for sixfold coordination is 0.414.

20.15b Verify that the radius ratios for eightfold coordination is 0.732.

20.16a From the data in Table 20.3 determine the radius of the smallest cation that can have (a) sixfold and (b) eightfold coordination with the O^{2-} ion.

20.16b From the data in Table 20.3 determine the radius of the smallest cation that can have (a) sixfold and (b) eightfold coordination with the K^+ ion.

20.17a Calculate the atomic packing factor for diamond.

20.17b Calculate the atomic packing factor for a side-centred (C) cubic unit cell.

20.18a Is there an expansion or a contraction as titanium transforms from hcp to body-centred cubic? The atomic radius of titanium is 145.8 pm in hcp but 142.5 pm in bcc.

20.18b Is there an expansion or a contraction as iron transforms from hcp to bcc? The atomic radius of iron is 126 pm in hcp but 122 pm in bcc.

20.19a In a Patterson synthesis, the spots correspond to the lengths and directions of the vectors joining the atoms in a unit cell. Sketch the pattern that would be obtained for a planar, triangular isolated BF_3 molecule.

20.19b In a Patterson synthesis, the spots correspond to the lengths and directions of the vectors joining the atoms in a unit cell. Sketch the pattern that would be obtained from the C atoms in an isolated benzene molecule.

20.20a What velocity should neutrons have if they are to have wavelength 50 pm?

20.20b Calculate the wavelength of neutrons that have reached thermal equilibrium by collision with a moderator at 300 K.

20.21a Derive the Born–Mayer equation (eqn 20.15) by calculating the energy at which $d(E_p + E_p^*)/dd = 0$, with E_p and E_p^* given by eqns 20.13 and 20.14, respectively.

20.21b Calculate the lattice enthalpy of MgBr_2 from the following data:

$$\Delta H/(\text{kJ mol}^{-1})$$

Sublimation of Mg(s)	+148
Ionization of Mg(g) to $\text{Mg}^{2+}(\text{g})$	+2187
Vaporization of $\text{Br}_2(\text{l})$	+31
Dissociation of $\text{Br}_2(\text{g})$	+193
Electron attachment to Br(g)	-331
Formation of $\text{MgBr}_2(\text{s})$ from Mg(s) and $\text{Br}_2(\text{l})$	-524

20.22a Cotton consists of the polymer cellulose, which is a linear chain of glucose molecules. The chains are held together by hydrogen bonding. When a cotton shirt is ironed, it is first moistened, then heated under pressure. Explain this process.

20.22b Sections of the solid fuel rocket boosters of the space shuttle *Challenger* were sealed together with O-ring rubber seals of circumference 11 m. These seals failed at 0°C , a temperature well above the crystallization temperature of the rubber. Speculate on why the failure occurred.

20.23a Young's modulus for polyethylene at room temperature is 1.2 GPa. What strain will be produced when a mass of 1.0 kg is suspended from a polyethylene thread of diameter 1.0 mm?

20.23b Young's modulus for iron at room temperature is 215 GPa. What strain will be produced when a mass of 10.0 kg is suspended from an iron wire of diameter 0.10 mm?

20.24a Poisson's ratio for polyethylene is 0.45. What change in volume takes place when a cube of polyethylene of volume 1.0 cm^3 is subjected to a uniaxial stress that produces a strain of 1.0 per cent?

20.24b Poisson's ratio for lead is 0.41. What change in volume takes place when a cube of lead of volume 1.0 dm^3 is subjected to a uniaxial stress that produces a strain of 2.0 per cent?

20.25a Is arsenic-doped germanium a p-type or n-type semiconductor?

20.25b Is gallium-doped germanium a p-type or n-type semiconductor?

20.26a The promotion of an electron from the valence band into the conduction band in pure TiO_2 by light absorption requires a wavelength of less than 350 nm. Calculate the energy gap in electronvolts between the valence and conduction bands.

20.26b The band gap in silicon is 1.12 eV. Calculate the minimum frequency of electromagnetic radiation that results in promotion of electrons from the valence to the conduction band.

20.27a The magnetic moment of CrCl_3 is $3.81\mu_{\text{B}}$. How many unpaired electrons does the Cr possess?

20.27b The magnetic moment of Mn^{2+} in its complexes is typically $5.3\mu_{\text{B}}$. How many unpaired electrons does the ion possess?

20.28a Calculate the molar susceptibility of benzene given that its volume susceptibility is -7.2×10^{-7} and its density 0.879 g cm^{-3} at 25°C .

20.28b Calculate the molar susceptibility of cyclohexane given that its volume susceptibility is -7.9×10^{-7} and its density 811 kg m^{-3} at 25°C .

20.29a According to Lewis theory, an O_2 molecule should be diamagnetic. However, experimentally it is found that $\chi_m/(m^3 \text{ mol}^{-1}) = (1.22 \times 10^{-5} \text{ K})/T$. Determine the number of unpaired spins in O_2 . How is the problem of the Lewis structure resolved?

20.29b Predict the molar susceptibility of nitrogen dioxide at 298 K. Why does the molar susceptibility of a sample of nitrogen dioxide gas decrease as it is compressed?

20.30a Data on a single crystal of MnF_2 give $\chi_m = 0.1463 \text{ cm}^3 \text{ mol}^{-1}$ at 294.53 K. Determine the effective number of unpaired electrons in this compound and compare your result with the theoretical value.

20.30b Data on a single crystal of $\text{NiSO}_4 \cdot 7\text{H}_2\text{O}$ give $\chi_m = 6.00 \times 10^{-8} \text{ m}^3 \text{ mol}^{-1}$ at 298 K. Determine the effective number of unpaired electrons in this compound and compare your result with the theoretical value.

20.31a Estimate the spin-only molar susceptibility of $\text{CuSO}_4 \cdot 5\text{H}_2\text{O}$ at 25°C .

20.31b Estimate the spin-only molar susceptibility of $\text{MnSO}_4 \cdot 4\text{H}_2\text{O}$ at 298 K.

20.32a Approximately how large must the magnetic induction, B , be for the orientational energy of an $S = 1$ system to be comparable to kT at 298 K?

20.32b Estimate the ratio of populations of the M_S states of a system with $S = 1$ in 15.0 T at 298 K.

Problems*

Numerical problems

20.1 In the early days of X-ray crystallography there was an urgent need to know the wavelengths of X-rays. One technique was to measure the diffraction angle from a mechanically ruled grating. Another method was to estimate the separation of lattice planes from the measured density of a crystal. The density

of NaCl is 2.17 g cm^{-3} and the (100) reflection using $\text{Pd}K_\alpha$ radiation occurred at 6.0° . Calculate the wavelength of the X-rays.

20.2 The element polonium crystallizes in a cubic system. Bragg reflections, with X-rays of wavelength 154 pm, occur at $\sin \theta = 0.225, 0.316$, and 0.388 from the (100), (110), and (111) sets of planes. The separation between the

* Problems denoted with the symbol ‡ were supplied by Charles Trapp and Carmen Giunta.

sixth and seventh lines observed in the powder diffraction pattern is larger than between the fifth and sixth lines. Is the unit cell simple, body-centred, or face-centred? Calculate the unit cell dimension.

20.3 The unit cell dimensions of NaCl, KCl, NaBr, and KBr, all of which crystallize in face-centred cubic lattices, are 562.8 pm, 627.7 pm, 596.2 pm, and 658.6 pm, respectively. In each case, anion and cation are in contact along an edge of the unit cell. Do the data support the contention that ionic radii are constants independent of the counter-ion?

20.4 The powder diffraction patterns of (a) tungsten, (b) copper obtained in a camera of radius 28.7 mm are shown in Fig. 20.69. Both were obtained with 154 pm X-rays and the scales are marked. Identify the unit cell in each case, and calculate the lattice spacing. Estimate the metallic radii of W and Cu.

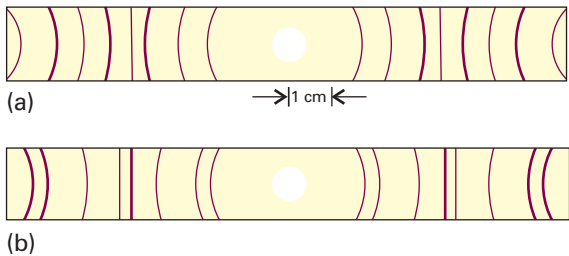


Fig. 20.69

20.5 Elemental silver reflects X-rays of wavelength 154.18 pm at angles of 19.076°, 22.171°, and 32.256°. However, there are no other reflections at angles of less than 33°. Assuming a cubic unit cell, determine its type and dimension. Calculate the density of silver.

20.6 Genuine pearls consist of concentric layers of calcite crystals (CaCO_3) in which the trigonal axes are oriented along the radii. The nucleus of a cultured pearl is a piece of mother-of-pearl that has been worked into a sphere on a lathe. The oyster then deposits concentric layers of calcite on the central seed. Suggest an X-ray method for distinguishing between real and cultured pearls.

20.7 In their book *X-rays and crystal structures* (which begins 'It is now two years since Dr. Laue conceived the idea . . .') the Braggs give a number of simple examples of X-ray analysis. For instance, they report that the reflection from (100) planes in KCl occurs at 5° 23', but for NaCl it occurs at 6° 0' for X-rays of the same wavelength. If the side of the NaCl unit cell is 564 pm, what is the side of the KCl unit cell? The densities of KCl and NaCl are 1.99 g cm^{-3} and 2.17 g cm^{-3} respectively. Do these values support the X-ray analysis?

20.8 Calculate the coefficient of thermal expansion of diamond given that the (111) reflection shifts from 22° 2' 25" to 21° 57' 59" on heating a crystal from 100 K to 300 K and 154.0562 pm X-rays are used.

20.9 The carbon–carbon bond length in diamond is 154.45 pm. If diamond were considered to be a close-packed structure of hard spheres with radii equal to half the bond length, what would be its expected density? The diamond lattice is face-centred cubic and its actual density is 3.516 g cm^{-3} . Can you explain the discrepancy?

20.10 The volume of a monoclinic unit cell is $abc \sin \beta$. Naphthalene has a monoclinic unit cell with two molecules per cell and sides in the ratio 1.377:1:1.436. The angle β is 122° 49' and the density of the solid is 1.152 g cm^{-3} . Calculate the dimensions of the cell.

20.11 The structures of crystalline macromolecules may be determined by X-ray diffraction techniques by methods similar to those for smaller molecules. Fully crystalline polyethylene has its chains aligned in an orthorhombic unit cell of dimensions 740 pm \times 493 pm \times 253 pm. There are two repeating

CH_2CH_2 units per unit cell. Calculate the theoretical density of fully crystalline polyethylene. The actual density ranges from 0.92 to 0.95 g cm^{-3} .

20.12 Construct the electron density along the x -axis of a crystal given the following structure factors:

h	0	1	2	3	4	5	6	7	8	9
F_h	+30.0	+8.2	+6.5	+4.1	+5.5	-2.4	+5.4	+3.2	-1.0	+1.1
h	10	11	12	13	14	15				
F_h	+6.5	+5.2	-4.3	-1.2	+0.1	+2.1				

20.13 The scattering of electrons or neutrons from a pair of nuclei separated by a distance R_{ij} and orientated at a definite angle to the incident beam can be calculated. When the molecule consists of a number of atoms, we sum over the contribution from all pairs, and find that the total intensity has an angular variation given by the *Wierl equation*:

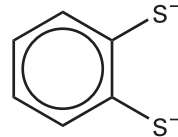
$$I(\theta) = \sum_{ij} f_i f_j \frac{\sin sR_{ij}}{sR_{ij}} \quad s = \frac{4\pi}{\lambda} \sin \frac{1}{2}\theta$$

where λ is the wavelength of the electrons in the beam and θ is the scattering angle. The *electron scattering factor*, f , is a measure of the intensity of the electron scattering powers of the atoms. (a) Predict from the Wierl equation the positions of the first maximum and first minimum in the neutron and electron diffraction patterns of a Br_2 molecule obtained with neutrons of wavelength 78 pm wavelength and electrons of wavelength 4.0 pm.

(b) Use the Wierl equation to predict the appearance of the 10.0 keV electron diffraction pattern of CCl_4 with an (as yet) underdetermined C–Cl bond length but of known tetrahedral symmetry. Take $f_{\text{Cl}} = 17f$ and $f_{\text{C}} = 6f$ and note that $R(\text{Cl}, \text{Cl}) = (8/3)^{1/2} R(\text{C}, \text{Cl})$. Plot I/f^2 against positions of the maxima, which occurred at 3° 0', 5° 22', and 7° 54', and minima, which occurred at 1° 46', 4° 6', 6° 40', and 9° 10'. What is the C–Cl bond length in CCl_4 ?

20.14‡ B.A. Bovenzi and G.A. Pearse, Jr. (*J. Chem. Soc. Dalton Trans.* 2793 (1997)) synthesized coordination compounds of the tridentate ligand pyridine-2,6-diamidoxime ($\text{C}_7\text{H}_9\text{N}_5\text{O}_2$). The compound, which they isolated from the reaction of the ligand with CuSO_4 (aq), did not contain a $[\text{Cu}(\text{C}_7\text{H}_9\text{N}_5\text{O}_2)_2]^{2+}$ complex cation as expected. Instead, X-ray diffraction analysis revealed a linear polymer of formula $[\text{Cu}(\text{Cu}(\text{C}_7\text{H}_9\text{N}_5\text{O}_2)(\text{SO}_4) \cdot 2\text{H}_2\text{O}]_n$, which features bridging sulfate groups. The unit cell was primitive monoclinic with $a = 1.0427$ nm, $b = 0.8876$ nm, $c = 1.3777$ nm, and $\beta = 93.254^\circ$. The mass density of the crystals is 2.024 g cm^{-3} . How many monomer units are there per unit cell?

20.15‡ D. Sellmann, M.W. Wemple, W. Donaubauer, and F.W. Heinemann (*Inorg. Chem.* 36, 1397 (1997)) describe the synthesis and reactivity of the ruthenium nitrido compound $[\text{N}(\text{C}_4\text{H}_9)_4][\text{Ru}(\text{N})(\text{S}_2\text{C}_6\text{H}_4)_2]$. The ruthenium complex anion has the two 1,2-benzenedithiolate ligands (**3**) at the base of a rectangular pyramid and the nitrido ligand at the apex. Compute the mass density of the compound given that it crystallizes into an orthorhombic unit cell with $a = 3.6881$ nm, $b = 0.9402$ nm, and $c = 1.7652$ nm and eight formula units per cell. Replacing the ruthenium with an osmium results in a compound with the same crystal structure and a unit cell with a volume less than 1 per cent larger. Estimate the mass density of the osmium analogue.



3

20.16 Aided by the Born–Mayer equation for the lattice enthalpy and a Born–Haber cycle, show that formation of CaCl is an exothermic process (the sublimation enthalpy of $\text{Ca}(s)$ is 176 kJ mol⁻¹). Show that an explanation

for the nonexistence of CaCl can be found in the reaction enthalpy for the reaction $2\text{CaCl(s)} \rightarrow \text{Ca(s)} + \text{CaCl}_2$.

20.17 In an intrinsic semiconductor, the band gap is so small that the Fermi–Dirac distribution results in some electrons populating the conduction band. It follows from the exponential form of the Fermi–Dirac distribution that the conductance G , the inverse of the resistance (with units of siemens, $1\text{ S} = 1\text{ }{\Omega}^{-1}$), of an intrinsic semiconductor should have an Arrhenius-like temperature dependence, shown in practice to have the form $G = G_0 e^{-E_g/2kT}$, where E_g is the band gap. The conductance of a sample of germanium varied with temperature as indicated below. Estimate the value of E_g .

T/K	312	354	420
G/S	0.0847	0.429	2.86

20.18 Here we investigate quantitatively the spectra of molecular solids. We begin by considering a dimer, with each monomer having a single transition with transition dipole moment μ_{mon} and wavenumber \tilde{v}_{mon} . We assume that the ground state wavefunctions are not perturbed as a result of dimerization and then write the dimer excited state wavefunctions Ψ_i as linear combinations of the excited state wavefunctions ψ_1 and ψ_2 of the monomer: $\Psi_i = c_j \psi_1 + c_k \psi_2$. Now we write the hamiltonian matrix with diagonal elements set to the energy between the excited and ground state of the monomer (which, expressed as a wavenumber, is simply \tilde{v}_{mon}), and off-diagonal elements correspond to the energy of interaction between the transition dipoles. Using the arrangement discussed in *Illustration 20.1*, we write this interaction energy (as a wavenumber) as:

$$\beta = \frac{\mu_{\text{mon}}^2}{4\pi\epsilon_0 hc r^3} (1 - 3 \cos^2 \theta)$$

It follows that the hamiltonian matrix is

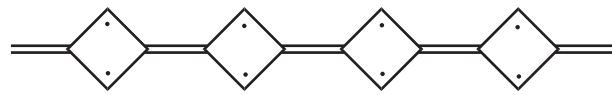
$$\hat{H} = \begin{pmatrix} \tilde{v}_{\text{mon}} & \beta \\ \beta & \tilde{v}_{\text{mon}} \end{pmatrix}$$

The eigenvalues of the matrix are the dimer transition wavenumbers \tilde{v}_1 and \tilde{v}_2 . The eigenvectors are the wavefunctions for the excited states of the dimer and have the form $\begin{pmatrix} c_j \\ c_k \end{pmatrix}$. (a) The intensity of absorption of incident radiation is proportional to the square of the transition dipole moment (Section 9.10). The monomer transition dipole moment is $\mu_{\text{mon}} = \int \psi_1^* \hat{\mu} \psi_0 d\tau = \int \psi_2^* \hat{\mu} \psi_0 d\tau$, where ψ_0 is the wavefunction of the monomer ground state. Assume that the dimer ground state may also be described by ψ_0 and show that the transition dipole moment μ_i of each dimer transition is given by $\mu_i = \mu_{\text{mon}}(c_j + c_k)$. (b) Consider a dimer of monomers with $\mu_{\text{mon}} = 4.00\text{ D}$, $\tilde{v}_{\text{mon}} = 25\,000\text{ cm}^{-1}$, and $r = 0.5\text{ nm}$. How do the transition wavenumbers \tilde{v}_1 and \tilde{v}_2 vary with the angle θ ? The relative intensities of the dimer transitions may be estimated by calculating the ratio μ_2^2/μ_1^2 . How does this ratio vary with the angle θ ? (c) Now expand the treatment given above to a chain of N monomers ($N = 5, 10, 15$, and 20), with $\mu_{\text{mon}} = 4.00\text{ D}$, $\tilde{v}_{\text{mon}} = 25\,000\text{ cm}^{-1}$, and $r = 0.5\text{ nm}$. For simplicity, assume that $\theta = 0$ and that only nearest neighbours interact with interaction energy V . For example the hamiltonian matrix for the case $N = 4$ is

$$\hat{H} = \begin{pmatrix} \tilde{v}_{\text{mon}} & V & 0 & 0 \\ V & \tilde{v}_{\text{mon}} & V & 0 \\ 0 & V & \tilde{v}_{\text{mon}} & V \\ 0 & 0 & V & \tilde{v}_{\text{mon}} \end{pmatrix}$$

How does the wavenumber of the lowest energy transition vary with size of the chain? How does the transition dipole moment of the lowest energy transition vary with the size of the chain?

20.19* J.J. Dannenberg, D. Liottard, P. Halvick, and J.C. Rayez (*J. Phys. Chem.* **100**, 9631 (1996)) carried out theoretical studies of organic molecules consisting of chains of unsaturated four-membered rings. The calculations



4

suggest that such compounds have large numbers of unpaired spins, and that they should therefore have unusual magnetic properties. For example, the lowest-energy state of the five-ring compound $\text{C}_{22}\text{H}_{14}$ (4) is computed to have $S = 3$, but the energies of $S = 2$ and $S = 4$ structures are each predicted to be 50 kJ mol^{-1} higher in energy. Compute the molar magnetic susceptibility of these three low-lying levels at 298 K. Estimate the molar susceptibility at 298 K if each level is present in proportion to its Boltzmann factor (effectively assuming that the degeneracy is the same for all three of these levels).

20.20 Lead has $T_c = 7.19\text{ K}$ and $H_c = 63\,901\text{ A m}^{-1}$. At what temperature does lead become superconducting in a magnetic field of 20 kA m^{-1} ?

20.21* P.G. Radaelli, M. Marezio, M. Perroux, S. de Brion, J.L. Tholence, Q. Huang, and A. Santoro (*Science* **265**, 380 (1994)) report the synthesis and structure of a material that becomes superconducting at temperatures below 45 K. The compound is based on a layered compound $\text{Hg}_2\text{Ba}_2\text{YCu}_2\text{O}_{8-\delta}$, which has a tetragonal unit cell with $a = 0.38606\text{ nm}$ and $c = 2.8915\text{ nm}$; each unit cell contains two formula units. The compound is made superconducting by partially replacing Y by Ca, accompanied by a change in unit cell volume by less than 1 per cent. Estimate the Ca content x in superconducting $\text{Hg}_2\text{Ba}_2\text{Y}_{1-x}\text{Ca}_x\text{Cu}_2\text{O}_{7.55}$ given that the mass density of the compound is 7.651 g cm^{-3} .

Theoretical problems

20.22 Show that the separation of the (hkl) planes in an orthorhombic crystal with sides a , b , and c is given by eqn 20.3.

20.23 Show that the volume of a triclinic unit cell of sides a , b , and c and angles α , β , and γ is

$$V = abc(1 - \cos^2 \alpha - \cos^2 \beta - \cos^2 \gamma + 2 \cos \alpha \cos \beta \cos \gamma)^{1/2}$$

Use this expression to derive expressions for monoclinic and orthorhombic unit cells. For the derivation, it may be helpful to use the result from vector analysis that $V = \mathbf{a} \cdot \mathbf{b} \times \mathbf{c}$ and to calculate V^2 initially.

20.24 Calculate the packing fractions of (a) a primitive cubic lattice, (b) a bcc unit cell, (c) an fcc unit cell.

20.25 The coordinates of the four I atoms in the unit cell of KIO_4 are $(0,0,0)$, $(0,\frac{1}{2},\frac{1}{2})$, $(\frac{1}{2},\frac{1}{2},\frac{1}{2})$, $(\frac{1}{2},0,\frac{3}{4})$. By calculating the phase of the I reflection in the structure factor, show that the I atoms contribute no net intensity to the (114) reflection.

20.26 The coordinates, in units of a , of the A atoms, with scattering factor f_A , in a cubic lattice are $(0,0,0)$, $(0,1,0)$, $(0,0,1)$, $(0,1,1)$, $(1,0,0)$, $(1,1,0)$, $(1,0,1)$, and $(1,1,1)$. There is also a B atom, with scattering factor f_B , at $(\frac{1}{2},\frac{1}{2},\frac{1}{2})$. Calculate the structure factors F_{hkl} and predict the form of the powder diffraction pattern when (a) $f_A = f$, $f_B = 0$, (b) $f_B = \frac{1}{2}f_A$, and (c) $f_A = f_B = f$.

20.27 For an isotropic substance, the moduli and Poisson's ratio may be expressed in terms of two parameters λ and μ called the Lamé constants:

$$E = \frac{\mu(3\lambda + 2\mu)}{\lambda + \mu} \quad K = \frac{3\lambda + 2\mu}{3} \quad G = \mu \quad V_p = \frac{\lambda}{3(\lambda + \mu)}$$

Use the Lamé constants to confirm the relations between G , K , and E given in eqn 20.18.

20.28 When energy levels in a band form a continuum, the density of states $\rho(E)$, the number of levels in an energy range divided by the width of the range, may be written as $\rho(E) = dk/dE$, where dk is the change in the quantum number k and dE is the energy change. (a) Use eqn 20.21 to show that

$$\rho(E) = -\frac{(N+1)/2\pi\beta}{\left\{1 - \left(\frac{E-\alpha}{2\beta}\right)^2\right\}^{1/2}}$$

where k , N , α , and β have the meanings described in Section 20.9. (b) Use the expression above to show that $\rho(E)$ becomes infinite as E approaches $\alpha \pm 2\beta$. That is, show that the density of states increases towards the edges of the bands in a one-dimensional metallic conductor.

20.29 The treatment in Problem 20.28 applies only to one-dimensional solids. In three dimensions, the variation of density of states is more like that shown in Fig. 20.70. Account for the fact that in a three-dimensional solid the greatest density of states lies near the centre of the band and the lowest density at the edges.

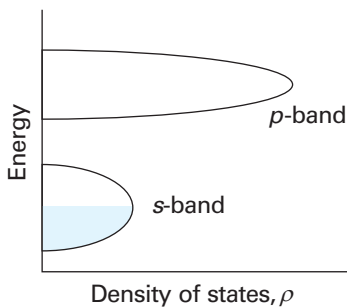


Fig. 20.70

20.30 Show that, if a substance responds nonlinearly to two sources of radiation, one of frequency ω_1 and the other of frequency ω_2 , then it may give rise to radiation of the sum and difference of the two frequencies. This nonlinear optical phenomenon is known as *frequency mixing* and is used to expand the wavelength range of lasers in laboratory applications, such as spectroscopy and photochemistry.

20.31 The magnetizability, ξ , and the volume and molar magnetic susceptibilities can be calculated from the wavefunctions of molecules. For instance, the magnetizability of a hydrogenic atom is given by the expression $\xi = -(e^2/6m_e)\langle r^2 \rangle$, where $\langle r^2 \rangle$ is the (expectation) mean value of r^2 in the atom. Calculate ξ and χ_m for the ground state of a hydrogenic atom.

20.32 Nitrogen dioxide, a paramagnetic compound, is in equilibrium with its dimer, dinitrogen tetroxide, a diamagnetic compound. Derive an expression in terms of the equilibrium constant, K , for the dimerization to show how the molar susceptibility varies with the pressure of the sample. Suggest how the susceptibility might be expected to vary as the temperature is changed at constant pressure.

20.33 An NO molecule has thermally accessible electronically excited states. It also has an unpaired electron, and so may be expected to be paramagnetic. However, its ground state is not paramagnetic because the magnetic moment of the orbital motion of the unpaired electron almost exactly cancels the spin magnetic moment. The first excited state (at 121 cm^{-1}) is paramagnetic because the orbital magnetic moment adds to, rather than cancels, the spin magnetic moment. The upper state has a magnetic moment of $2\mu_B$. Because the upper state is thermally accessible, the paramagnetic susceptibility of NO shows a pronounced temperature dependence even near room temperature. Calculate the molar paramagnetic susceptibility of NO and plot it as a function of temperature.

Applications: to biochemistry and nanoscience

20.34 Although the crystallization of large biological molecules may not be as readily accomplished as that of small molecules, their crystal lattices are no different. Tobacco seed globulin forms face-centred cubic crystals with unit cell dimension of 12.3 nm and a density of 1.287 g cm^{-3} . Determine its molar mass.

20.35 What features in an X-ray diffraction pattern suggest a helical conformation for a biological macromolecule? Use Fig. 20.26 to deduce as much quantitative information as you can about the shape and size of a DNA molecule.

20.36 A transistor is a semiconducting device that is commonly used either as a switch or an amplifier of electrical signals. Prepare a brief report on the design of a nanometre-sized transistor that uses a carbon nanotube as a component. A useful starting point is the work summarized by Tans *et al.* *Nature* **393**, 49 (1998).

20.37 The tip of a scanning tunnelling microscope can be used to move atoms on a surface. The movement of atoms and ions depends on their ability to leave one position and stick to another, and therefore on the energy changes that occur. As an illustration, consider a two-dimensional square lattice of univalent positive and negative ions separated by 200 pm , and consider a cation on top of this array. Calculate, by direct summation, its Coulombic interaction when it is in an empty lattice point directly above an anion.



PART 3 Change

Part 3 considers the processes by which change occurs. We prepare the ground for a discussion of the rates of reactions by considering the motion of molecules in gases and in liquids. Then we establish the precise meaning of reaction rate, and see how the overall rate, and the complex behaviour of some reactions, may be expressed in terms of elementary steps and the atomic events that take place when molecules meet. Characteristic physical and chemical events take place at surfaces, including catalysis, and we see how to describe them. A special type of surface is that of an electrode, and we shall see how to describe and understand the rate at which electrons are transferred between an electrode and species in solution.

- 21** Molecules in motion
- 22** The rates of chemical reactions
- 23** The kinetics of complex reactions
- 24** Molecular reaction dynamics
- 25** Processes at solid surfaces

This page intentionally left blank